HERON is jointly edited by:
STEVIN-LABORATORY of the
faculty of Civil Engineering,
Delft University of Technology,
Delft, The Netherlands
and
TNO BUILDING AND
CONSTRUCTION RESEARCH.
Rijswijk (ZH), The Netherlands
HERON contains contributions
based mainly on research work
performed in these laboratories
on strength of materials, structures
and materials science.

ISSN 0046-7316

This publication has been issued in close co-operation with the Netherlands Technology Foundation (STW)

Secretary:
J. G. M. van Mier
Stevinweg 1
P.O. Box 5048
2600 GA Delft, The Netherlands
Tel. 0031-15-784578
Fax 0031-15-611465
Telex 38151 BUTUD

HERON vol. 38
1993
no. 4

Contents

ASPECTS OF ROBUST COMPUTATIONAL MODELING FOR PLAIN AND REINFORCED CONCRETE

P. H. Feenstra
R. de Borst
Delft University of Technology
Faculty of Civil Engineering

Publication in HERON since 1970

Abstract

The problems commonly encountered in the numerical analysis of reinforced structures are often related to biaxial stress states in the structure. In this study this problem is solved with the formulation of a composite plasticity model which describes both cracking and crushing of concrete within the framework of plasticity theory. The other issue which is treated in this study is the rational modeling of the interaction between concrete and reinforcement.

Keywords: Finite element analysis, fracture mechanics, softening, reinforced concrete.

Aspects of Robust Computational Models for Plain and Reinforced Concrete

1. Introduction

Reinforced concrete is one of the most commonly used materials in civil engineering with applications in all kinds of structures, such as high rise buildings, cooling towers and offshore platforms. The design of these structures is usually based on a linear-elastic analysis to calculate the internal forces in the structure which are then used to design the reinforcement and the details of the structure using code provisions. These codes are usually based on an empirical approach, using experimental data, and provide design rules to satisfy safety and serviceability requirements. Although the design of reinforced concrete structures based on a linear-elastic stress analysis is adequate and reliable in most cases, for complex structures under complex loading conditions, nonlinear finite element analyses are often required. With these analyses, information can be obtained regarding the ultimate load capacity and the post-failure behavior of the structure.

The behavior of concrete structures is characterized by a reduction of the load-carrying capacity with increasing deformations after reaching a certain limit load. This global behavior is usually caused by a material behavior which is described as strain softening and occurs in tension and in compression. Due to this softening behavior, the deformations tend to localize in a small part of the structure which can introduce mesh-dependent responses in finite element calculations. This deficiency can partially be solved by relating the constitutive model to a fracture energy and to the geometry of the finite element mesh via an equivalent length. In reinforced concrete generally a number of cracks will develop in the structure due to the bond action between concrete and reinforcement. This results in a redistribution of the tensile load from concrete to reinforcement. This phenomenon is called tension-stiffening, because the response is stiffer than the response with a brittle fracture approach. The tension-stiffening is closely related to the tension-softening in plain concrete and the controversy between tension-softening and tension-stiffening approaches seems to have been exaggerated in the past.

An issue which can cause numerical difficulties is the biaxial stress state, especially in tension-compression. The numerical problems are mainly due to the fact that the nonlinear behavior in tension, viz. cracking, is treated by a different constitutive model than the nonlinear behavior in compression, viz. crushing. These different constitutive models are treated in different algorithms and a local iteration on a constitutive level is

necessary to meet both the cracking and the crushing conditions. This local iteration process can result in an oscillating numerical process if both cracking and crushing occur in the same integration point. Because tension-compression stress states often occur in reinforced concrete, this problem is encountered frequently.

The behavior of reinforced concrete is highly nonlinear which is caused by mechanisms such as cracking, crushing, creep and shrinkage of concrete, but is also caused by interaction between reinforcement and concrete. Because all these mechanisms are interacting, it is not realistic to try to formulate a constitutive model which incorporates all these mechanisms, but a model has to be formulated which adequately describes the behavior of a structure within the range of application which has been restricted in advance. Although the constitutive models which are developed within this phenomenological approach are usually simplified representations of the real behavior of a material, it is believed that more insight can be gained by tracing the entire response of a structure in this manner, than modeling a structure with highly sophisticated material models which do not result in a converged solution after failure load. Since structural failure cannot be identified with divergence of the iterative procedure, the principal aim of this study is to discuss robust algorithms in order to provide the structural engineer with reliable numerical tools.

2. Material model for plain and reinforced concrete

In experiments on plain concrete, two types of failure are observed which are both characterized by the formation of cracks in the material. When a concrete specimen is loaded in tension the response is nearly linear up to the maximum load. At peak load existing cracks at micro-level due to hydratation and drying shrinkage, see Wittman (1983), localize in a narrow band and a macro-crack develops in the process zone which is attended by a decrease of the external load, Hordijk (1991). Recently, also the compressive failure of concrete has been recognized to be governed by cracking of concrete, Van Mier (1984), Vonk (1992). The crack growth at the micro-level causes the softening behavior of concrete under compression. Until about 30 % of the maximum compressive strength the material behaves linear-elastically because pre-existing micro cracks are stable and do not propagate. These micro cracks start to grow if the specimen is loaded further and up to the maximum compressive strength the formation of combined mortar and bond cracks have been observed. After the maximum compressive strength macro cracks develop because the micro cracks localize in narrow bands which is attended by a decrease of the external applied load.

The behavior of reinforced concrete is also characterized by the formation of cracks in the material. The major difference with plain concrete is the bond action between concrete and reinforcement which results in the formation of a number of cracks and a

redistribution of internal stresses from concrete to reinforcement.

The constitutive behavior will be modeled according to a phenomenological approach in which the observed mechanisms are modeled in such a fashion that simulations with the developed material model are in reasonable agreement with the experiments.

2.1 Discretization aspects

The constitutive behavior of concrete will be modeled with a smeared model in which the damaged material is still considered as a continuum in which the notions of stress and strain apply. With this assumption, the localized damage can be represented by an internal damage parameter, denoted as κ, which is related by an equivalent length to the released energy per unit cracked area, G_f. In a finite element calculation this equivalent length should correspond to a representative dimension of the mesh size, as pointed out by many authors, see Bažant and Oh (1983), Crisfield (1984), Willam, Pramono and Sture (1986), Rots (1988) and Oliver (1989). The equivalent length, denoted by h, depends in general on the chosen element type, element size, element shape, integration scheme and even on the particular problem considered. In this study it is assumed that the equivalent length is related to the area of an element, as follows

$$h = \alpha_h \sqrt{A_e} = \alpha_h \left(\sum_{\xi=1}^{n_\xi} \sum_{\eta=1}^{n_\eta} \det(\boldsymbol{J})\, w_\xi\, w_\eta \right)^{1/2} \tag{1}$$

in which w_ξ and w_η the weight factors of the Gaussian integration rule as it is tacitly assumed that the elements are always integrated numerically. The local, isoparametric coordinates of the integration points are given by ξ and η. The factor α_h is a modification factor which is equal to one for quadratic elements and equal to $\sqrt{2}$ for linear elements, see Rots (1988). The equivalent length calculated with this formula is accurate when the mesh is not distorted too much and when most cracks are aligned with the mesh lines. For most practical applications the formula for the equivalent length, eq.(1), gives a good approximation.

The accumulated damage in the material will be represented by an internal parameter κ which is assumed to be determined by the inelastic work using a work-hardening hypothesis. The inelastic work rate $\dot{W}_c$ is defined by

$$\dot{W}_c = \boldsymbol{\sigma}^T \dot{\boldsymbol{\varepsilon}}_c = \bar{\sigma}(\kappa)\, \dot{\kappa} \tag{2}$$

in which $\dot{\boldsymbol{\varepsilon}}_c$ the inelastic strain rate vector and $\bar{\sigma}(\kappa)$ an equivalent stress as a function of the internal parameter κ. The inelastic work g_f is then defined by the integral

$$g_f = \int_{t=0}^{t=\infty} \dot{W}_c \, d\tau = \int_{\kappa=0}^{\kappa=\infty} \bar{\sigma}(\kappa) \, d\kappa \tag{3}$$

Assuming that the inelastic work g_f is distributed uniformly over the equivalent length, the relation between the fracture energy G_f and the work g_f is given by

$$g_f = \frac{G_f}{h} \tag{4}$$

This results in a material model which is related to the energy which has to be dissipated due to the irreversible damage in the material. The concept of an equivalent length has been used extensively in the analysis of concrete structures. In this study, this concept will also be used to model the compressive softening behavior of concrete, although it is recognized that this mechanism is perhaps more related to the volume of the elements than to a representative length of the elements.

The nonlinear material behavior is now completely governed by an assumed equivalent stress - internal parameter relation, the $\bar{\sigma} - \kappa$ relation, which will be discussed in the next paragraph for both tension and compression.

2.2 Uniaxial behavior of plain concrete

The design of concrete structures is usually based on a grade of concrete which corresponds to a specific value of the characteristic compressive strength f_{ck}, which is determined with compressive tests on concrete cylinders 150 $[mm]$ in diameter and 300 $[mm]$ in height, see CEB-FIP model code (1990). A characteristic stress-displacement diagram for concrete loaded in compression is shown in Figure 1. For purposes of simulation and for an estimate of other concrete properties, the mean value of the compressive strength f_{cm} is needed, which is estimated by, see CEB-FIP model code (1990),

$$f_{cm} = f_{ck} + 8 \; [N/mm^2] \tag{5}$$

The initial behavior of concrete is modeled using a linear-elastic constitutive model which is completely defined by the Young's modulus and the Poisson ratio. The Young's modulus of concrete is defined as the initial slope of the stress-strain diagram and depends on the compressive strength and on the type of aggregate. For normal weight concrete the Young's modulus can be estimated from the CEB-FIP model code (1990) recommendation

$$E_c = 10^4 \, f_{cm}^{1/3} \; [N/mm^2] \tag{6}$$

The Poisson ratio ranges from 0.1 to 0.2. In this study a value of the Poisson ratio equal to 0.15 will be used. Concrete loaded in compression behaves linear-elastically up to approximately 30 % of the compressive strength and upon further loading a gradual

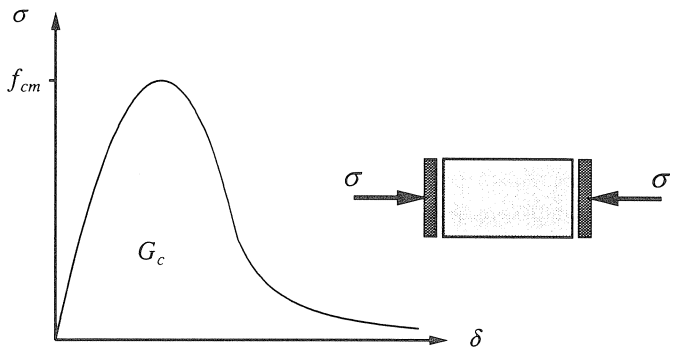

Figure 1 Concrete specimen under uniaxial compressive loading.

decrease of the stiffness is observed. If the deformation continues after the maximum compressive stress, the slope becomes negative and the descending branch of the stress-deformation curve characterizes the softening behavior of the concrete. The compression softening behavior of a concrete specimen is highly dependent upon the boundary conditions in the experiments and the size of the specimen, Van Mier (1984) and Vonk (1992). It is nevertheless assumed in this study that the compressive softening of concrete can be represented by a compressive fracture energy, denoted as G_c, which is assumed to be a material parameter. With this energy-based approach the compressive and tensile softening can be described within the same context which is plausible, because the underlying failure mechanisms are identical, viz. continuous crack growth at micro-level. Experimental data of the compressive fracture energy have been provided by Vonk (1992) who distinguishes a local compressive fracture energy which is constant and a continuum compressive fracture energy which is increasing with increasing specimen height. The total compressive fracture energy which has been found in the experiments ranges from 10 to 25 $[Nmm/mm^2]$ which is about 50-100 times the tensile fracture energy.

The compressive stress-strain behavior has been approximated by different functions, see e.g. Vecchio and Collins (1982), CEB-FIP model code (1990), but these relations are usually no energy-based formulations. In this study, the compressive constitutive model will be modeled either with ideal plastic behavior or with a compression softening model given by a parabolic equivalent stress-equivalent strain diagram according to Figure 2, which has been modified for the fracture energy-based model. The formulation of the equivalent stress reads

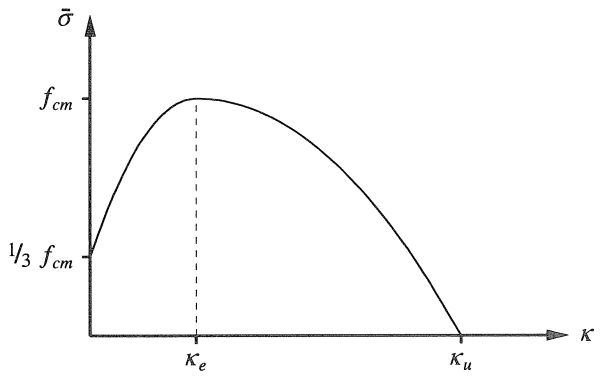

Figure 2 Compression softening model

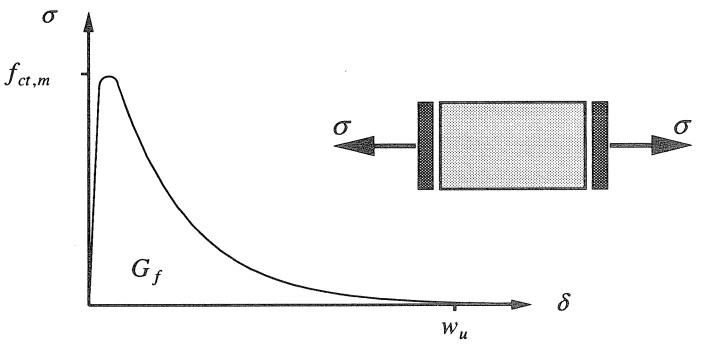

Figure 3 Concrete specimen under uniaxial tensile loading.

$$\bar{\sigma} = \begin{cases} \dfrac{f_{cm}}{3}\left(1 + 4\dfrac{\kappa}{\kappa_e} - 2\dfrac{\kappa^2}{\kappa_e^2}\right) & \text{if} \quad \kappa < \kappa_e \\ f_{cm}\left(1 - \dfrac{(\kappa - \kappa_e)^2}{(\kappa_u - \kappa_e)^2}\right) & \text{if} \quad \kappa_e \le \kappa < \kappa_u \end{cases} \tag{7}$$

The maximum compressive strength will be reached at an equivalent strain κ_e which is determined irrespective of element size or compressive fracture energy and reads

$$\kappa_e = \frac{4\, f_{cm}}{3\, E_c} \tag{8}$$

The maximum equivalent strain κ_u is related to the compressive fracture energy and the

element size and reads

$$\kappa_u = 1.5 \frac{G_c}{h\, f_{cm}} \tag{9}$$

A possible snap-back on constitutive level if the equivalent length becomes too large, has been avoided by the assumption that the ultimate equivalent strain κ_u is limited by

$$\kappa_u \geq 1.75\, \kappa_e \tag{10}$$

It is noted that the limiting case $\kappa_u = 1.75\, \kappa_e$ results in a steep descending branch after maximum stress.

The tensile strength of concrete is in accordance with the CEB-FIP model code (1990) related to the compressive strength. For the simulations performed in this study, the characteristic value of the tensile strength has been estimated by the CEB-FIP model code (1990) relationship

$$f_{ct,m} = 0.30\, f_{ck}^{\frac{2}{3}} \quad [N/mm^2] \tag{11}$$

A characteristic stress-deformation curve for concrete subjected to tensile loading is shown in Figure 3. Up to approximately 90 % of the maximum tensile load, the concrete behaves as a linear-elastic material. Then a macro-crack starts to develop and the stiffness reduces rapidly until the macro-crack cannot transfer any stress anymore. The released energy is then determined by the area under the stress-displacement diagram, which is equal to the fracture energy times the crack area. The fracture energy G_f is assumed to be a material parameter and is related to the compressive strength of the material f_{cm} and the maximum aggregate size $d_{\max}$, according to the CEB-FIP model code (1990) recommendations which reads

$$G_f = G_{F0}\, (\, f_{cm} \,/\, f_{cm0}\,)^{0.7} \quad [Nmm/mm^2] \tag{12}$$

where $f_{cm0} = 10[Nmm/mm^2]$. The base value for the fracture energy, G_{F0}, depends on the maximum aggregate size $d_{\max}$ as given in Table 1.

Table 1 Base values for fracture energy G_{F0} $[Nmm/mm^2]$ (CEB-FIP model code)

$d_{\max}$ $[mm]$	G_{F0} $[Nmm/mm^2]$
8	0.025
16	0.030
32	0.058

The material model up to the tensile strength $f_{ct,m}$ is assumed to be given by a linear-elastic model. The material model for tensile behavior after the tensile strength has been violated is depicted in Figure 4 as an equivalent stress - equivalent strain diagram. The

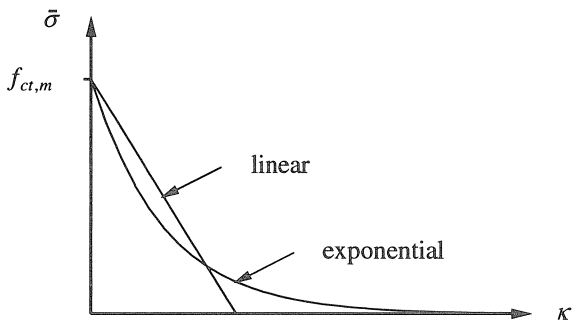

Figure 4 Tension-softening models

post-peak response is governed by the tensile fracture energy and the equivalent length. The tensile stress-strain relationship has been approximated by different functions, see e.g. CEB-FIP model code (1990), Hordijk (1991), and is one of the relevant features of the nonlinear tensile behavior of plain concrete, Rots (1988). In this study two different softening diagrams will be used, the linear and exponential diagram. For linear softening the equivalent stress as a function of the internal damage parameter κ is given by

$$\bar{\sigma} = f_{ct,m} \left(1 - \frac{\kappa}{\kappa_u} \right) \tag{13}$$

and for exponential softening

$$\bar{\sigma} = f_{ct,m} \, exp(- \kappa / \kappa_u) \tag{14}$$

The ultimate damage parameter κ_u is calculated by

$$\kappa_u = k \frac{G_f}{h \, f_{ct,m}} \tag{15}$$

with $k = 2$ for linear softening and $k = 1$ for exponential softening. The parameter κ_u is assumed constant during the analysis and is considered to be an *element-related material property* which can be calculated from the material properties, the tensile strength, the fracture energy and the element area represented by the equivalent length. The tensile fracture energy will be released in an element if the tensile strength is violated and the deformations localize in the element. With this approach the results which are obtained with the analysis are objective with regard to mesh refinement. It is however possible that the equivalent length of an element results in a snap-back in the constitutive model and the concept of objective fracture energy which has been assumed is no longer satisfied. In this case the strength limit has to be reduced in order to obtain an objective fracture energy by a sudden stress drop, resulting in brittle fracture, see Rots

(1988). The condition of a maximum equivalent length is given by

$$h \leq k \frac{G_f E}{f_{ct,m}^2} \tag{16}$$

If the condition of eq.(16) is violated, the tensile strength is reduced to

$$f_{ct,m} = \left(k \frac{G_f E}{h} \right)^{1/2} \tag{17}$$

2.3 Biaxial behavior of plain concrete

The constitutive behavior of concrete under biaxial states of stress is different from the constitutive behavior under uniaxial loading conditions. The influence of the biaxial stress state has been investigated up to peak stress to provide a biaxial failure criterion, where it becomes evident that the tensile strength of concrete is influenced by the lateral stress state. The experimental data of concrete subjected to proportional biaxial loading is shown in Figure 5, Kupfer and Gerstle (1973). The maximum compressive strength increases approximately 16 % under conditions of equal biaxial compression, and about 25 % increase is achieved at a stress ratio of $\sigma_1 / \sigma_2 = 0.5$. A lateral compressive stress decreases the tensile strength, which can be explained that a lateral compressive stress introduces tensile stresses at the micro-level due to the heterogeneity of the material, which increases the process of internal damage, Vonk (1992). A lateral tensile stress has no major influence on the tensile strength. The increase in the compressive strength under biaxial compression can be explained by internal friction and aggregate interlock. The failure envelop which can been derived from the data of Kupfer and Gerstle is also valid for nonproportional loading because the strength envelop seems to be largely independent of the loading path, Nelissen (1972), which confirms the notion that softening due to compressive or tensile external loadings has the same underlying failure mechanism, i.e. continuous crack growth at the microlevel. Experimental data on the softening behavior of concrete under biaxial stress conditions are scarce but there is a consensus of opinion that the softening of concrete is influenced by a biaxial stress state. For a multi-axial stress state it has been shown that softening is very sensitive for a confining pressure but in a biaxial stress state the concrete can always fail in the third direction which reduces the sensitivity to the confining pressure, Vonk (1992).

2.4 Uniaxial behavior of reinforced concrete

The uniaxial compressive behavior of reinforced concrete is usually modeled with the compressive material model for plain concrete which has been discussed previously.

The tensile behavior of reinforced concrete is not fundamentally different from plain concrete and is also governed by cracking in the concrete. A characteristic stress-

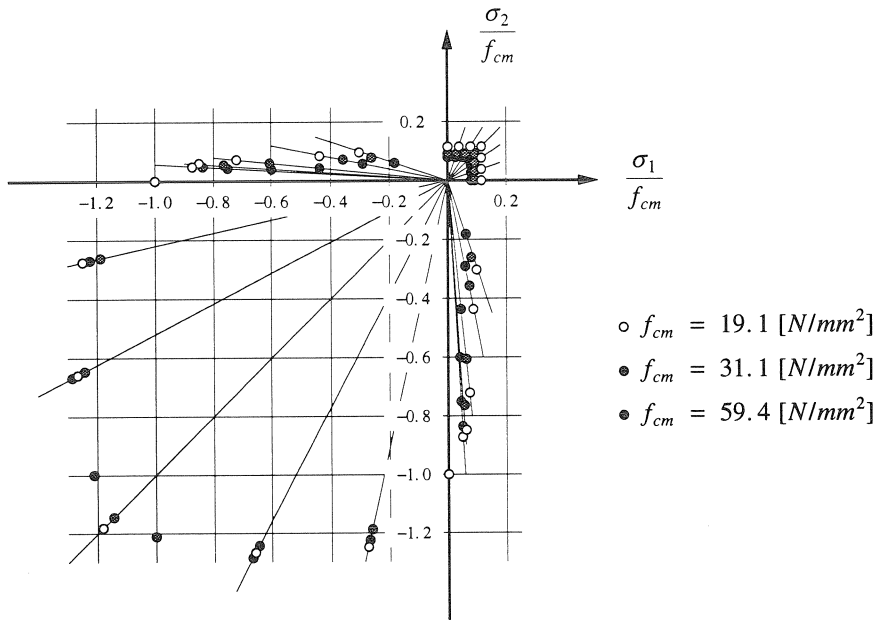

Figure 5 Biaxial strength of plain concrete, Kupfer and Gerstle (1973)

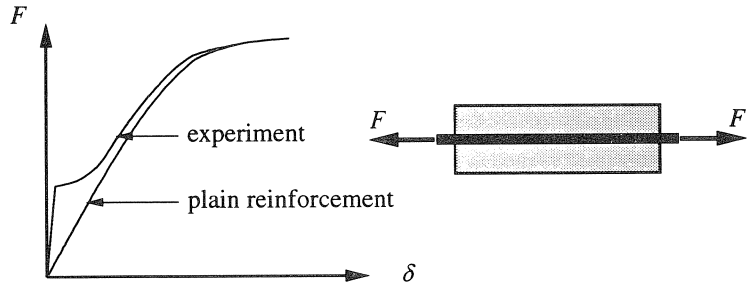

Figure 6 Reinforced concrete tensile member.

displacement diagram of a tension test is depicted in Figure 6. The existing cracks at the micro-level localize in a narrow band and a number of primary macro-cracks will develop. But due to bond between concrete and reinforcement, a gradual redistribution of internal forces from concrete to reinforcement is possible under the formation of secondary cracks until a stabilized crack pattern has developed. It is clear that the stiffness of the tension member is increased with reference to the reinforcing bar by the stiffness of the concrete. This effect is usually referred to in the literature as the tension-stiffening

effect. Different formulations have been put forward for this tension-stiffening phenomenon, but in most formulations no reference has been made to the fracture energy which is actually released in the material.

The total amount of released energy at stabilized cracking is determined by the fracture energy of a single crack G_f and the average crack spacing l_s. The transition between plain and reinforced concrete can be obtained by assuming that the released energy is at least equal to the fracture energy of the material and it is assumed that the released energy can be determined by

$$G_f^{rc} = \min\left\{ G_f \, , G_f \, \frac{h}{l_s} \right\} \tag{18}$$

with G_f the fracture energy of a single crack, h the equivalent length and l_s the average crack spacing. It is noted that if the equivalent lenght h is smaller than the average crack spacing l_s, the model is not valid. In general, the dimensions of the finite elements in simulations of reinforced concrete structures, and thus the equivalent length h, are much larger than the average crack spacing, l_s, which implies that the total amount of released energy is a number times the fracture energy. The average crack spacing is a function of the bar diameter, the concrete cover and the reinforcement ratio according to the CEB-FIP model code (1990), which reads

$$l_s = {}^2\!/_3 \, l_{s,max} = {}^2\!/_3 \, (\, 2 \, s_0 + \frac{\phi_s}{\alpha \, \rho_s} \,) \tag{19}$$

with s_0 the minimum bond length, ϕ_s the diameter of the reinforcement, a factor α equal to four for deformed bars and α equal to two for plain bars and the reinforcement ratio ρ_s given by

$$\rho_s = \frac{A_s}{A_c} \tag{20}$$

with A_s the total area of reinforcement and A_c the cross area of the tensile member. The minimum bond length s_0 is usually taken equal to 25 $[mm]$ in the absence of more precise data. A comparison of 132 experiments on tensile members, Braam (1990), showed that the average crack spacing given by eq.(19) is a good approximation of the experimentally observed crack spacing.

The formulas given in the previous paragraph are all related to the crack spacing in reinforced tensile members. Now, attention will be focused on the approximation of the released energy in plane two-dimensional structures like panels, reinforced with a reinforcing grid in two orthogonal directions. The crack spacing in panels is usually determined by treating a panel as a tensile member by the definition of an effective reinforcement ratio. If the reinforcement is supplied with a layer of a reinforcing grid, the average crack spacing is calculated with a modified expression of eq.(19),

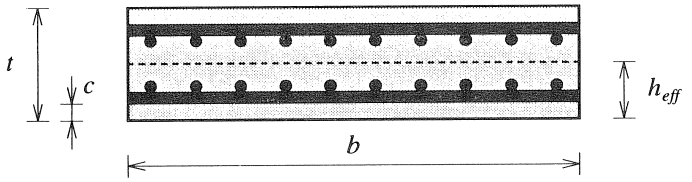

Figure 7 Concrete slab with two layers of reinforcement. Effective tension area according to CEB-FIP model code.

$$l_s = 2/3\, l_{s,max} = 2/3\, (2\, s_0 + \frac{\phi_s}{\alpha\, \rho_{s,eff}}) \tag{21}$$

with the effective reinforcement ratio $\rho_{s,eff}$ determined by

$$\rho_{s,eff} = \frac{A_s}{A_{c,eff}} \tag{22}$$

The effective tension area, $A_{c,eff} = h_{eff}\, b$, is estimated according to the CEB-FIP recommendations with the relation

$$h_{eff} = \min\left\{ 2.5\, (c + \frac{\phi_{eq}}{2}) \;,\; \frac{t}{2} \right\}$$

with c the concrete cover on the reinforcement, ϕ_{eq} the equivalent bar diameter of the reinforcement and t the thickness of the structure. These geometrical properties are shown in Figure 7. The effective tension area is calculated with the equivalent bar diameter of the reinforcing grid which is determined by

$$\phi_{eq} = \frac{\phi_{s,p}\, \rho_p + \phi_{s,q}\, \rho_q}{\rho_p + \rho_q} \tag{23}$$

with the reinforcement ratios ρ_p and ρ_q in the p- and q-directions of the reinforcing grid, respectively. The diameter of the reinforcement is given by $\phi_{s,p}$ and $\phi_{s,q}$ in the p- and q-direction. The average crack spacing can now be calculated in the two directions of the reinforcing grid. The crack spacing given by eq.(21) is based on the fact that the cracks form at right angles to the reinforcing direction. When the cracks form at inclined angles with the reinforcing directions this identity cannot be used to estimate the crack spacing. In these cases, the average crack spacing is calculated with the following expression according to the CEB-FIP model code (1990),

$$l_s = \left(\frac{|\cos\alpha|}{l_{s,p}} + \frac{|\sin\alpha|}{l_{s,q}} \right)^{-1} \tag{24}$$

where α denotes the angle between the reinforcement in the p-direction and the direction of the principal tensile stress at incipient cracking. The crack spacings predicted with eq.(24) are theoretically reasonable. For a structure reinforced equally in the p- and q-directions subjected to a pure shear loading, the cracks are forming at 45° to the p-direction and the crack spacing is $\frac{1}{2}\sqrt{2}$ times the crack spacing in the p- or q-direction. If the structure is only reinforced in the p-direction, the crack spacing for tension in the p-direction is equal to the value given by eq.(21). For tension in the q-direction the predicted crack spacing is equal to infinity, which implies that only one crack is formed in the structure. Comparison of the theoretical crack spacing with the experimental results of one-directionally reinforced structures shows that the trend of the crack spacing with increasing angle α is predicted correctly, but that the crack spacing is usually underestimated, Bhide and Collins (1987). This is due to the fact that only primary cracks have been observed with the secondary cracks being ignored. The expression of eq.(24) may be used according to the CEB-FIP model code (1990) when a more advanced model is not available.

As indicated in Figure 7, the reinforcement is usually applied in more layers with an arbitrary direction through the thickness of the structure. The average crack spacing of the structure is then determined by the smallest average crack spacing of all reinforcing grids. The average crack spacing in the case of different reinforcing grids with arbitrary directions will be given by by a modification of eq.(24),

$$l_s = \left(a_x + a_y \right)^{-1} \tag{25}$$

in which the factors a_x and a_y are determined by

$$a_x = \max\left(\frac{|\cos\alpha_j|}{l_{s,pj}}\right) \qquad a_y = \max\left(\frac{|\sin\alpha_j|}{l_{s,qj}}\right) \qquad j = 1, \cdots, n_{grid} \tag{26}$$

with α_j the angle between the reinforcement p-direction and the direction of the principal tensile stress at incipient cracking. It has tacitly been assumed that the cracks propagate through the entire thickness of the structure with no localization in the thickness direction. With this approach, the fracture energy in reinforced concrete can be assessed on the basis of the fracture energy of concrete, the reinforcement properties and the angle between reinforcement and the principal stress at incipient cracking. In this fashion, the tension-softening of reinforced concrete has been formulated in a rational manner.

After a stabilized crack pattern has developed, stresses are still transferred from

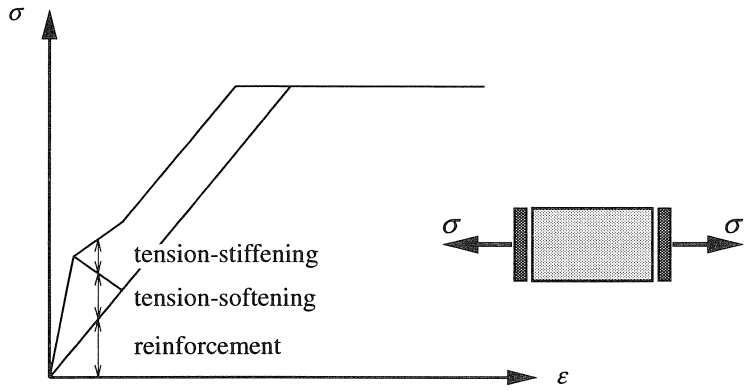

Figure 8 Constitutive model of reinforced concrete. Schematical representation.

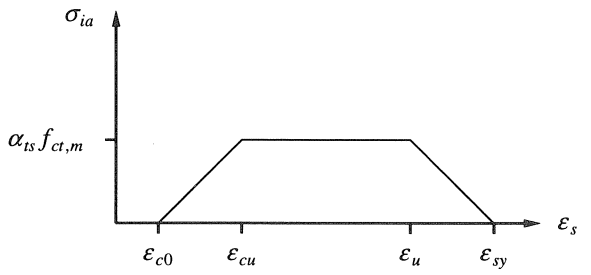

Figure 9 Tension-stiffening model.

reinforcement to concrete between the cracks due to the bond action which increases the total stiffness of the structure, see Figure 6. In this study it is assumed that the behavior of cracked, reinforced concrete loaded in tension can be considered as the superposition of the stiffness of plain concrete, a stiffness of the reinforcement and an additional stiffness due to bond between concrete and reinforcement which is referred to as the interaction contribution to the stiffness. This leads to the following summation of stress contributions

$$\boldsymbol{\sigma} = \boldsymbol{\sigma}_c + \boldsymbol{\sigma}_s + \boldsymbol{\sigma}_{ia} \tag{27}$$

with $\boldsymbol{\sigma}_c$ the stress contribution of the concrete, $\boldsymbol{\sigma}_s$ the contribution of the reinforcing steel, and $\boldsymbol{\sigma}_{ia}$ the interaction stress contribution due to tension-stiffening, see Figure 8. The additional stress due to tension-stiffening is assumed to be given as a function of the strain in the direction of the reinforcement and will be active on the effective tension

area defined in Figure 7. The interaction stress is assumed to be given by a tri-linear function according to Cervenka, Pukl and Eligehausen (1992) which is depicted in Figure 9. The interaction stress is only active if the strain in the reinforcement is larger than ε_{c0} which is determined by

$$\varepsilon_{c0} = \frac{f_{ct,m}}{E_c} \cos^2 \alpha \tag{28}$$

with α the angle between the direction of the reinforcement and the direction of the principal stress at incipient cracking. The factor ε_{cu} is determined by the crack spacing, the equivalent length of the element and the fracture energy of the concrete and is given by

$$\varepsilon_{cu} = k \cos^2 \alpha \frac{G_f^{rc}}{h\, f_{ct,m}} \tag{29}$$

with k equal to one for exponential softening and k equal to two for linear softening. The constant part of the diagram is a fraction of the tensile strength of the concrete with the factor α_{ts} as a rough approximation equal to the tensile strength, i.e $\alpha_{ts} = 1.0$. The tension-stiffening component is reduced near the yield strain of the reinforcement ε_{sy} in order to avoid an artificial increase of the yield stress of the reinforcement. The strain at which the tension-stiffening component is reduced is given by

$$\varepsilon_u = \varepsilon_{sy} - \frac{\alpha_{ts}\, f_{ct,m}}{\rho_{s,eff}\, E_s} \tag{30}$$

This tri-linear function will be used in this study, but further research to the actual function is necessary.

2.5 Biaxial behavior of reinforced concrete

The biaxial failure surface of plain concrete is also applicable to reinforced concrete, because the reinforcement is usually not activated in the linear-elastic state. The tension-tension behavior is not affected by the biaxial stress state and will be modeled with the uniaxial behavior in both directions. The compression-compression behavior will also be modeled with the uniaxial model. The compression-tension behavior of reinforced concrete is usually modified after cracking, because it is assumed that the compressive strength of concrete is affected by cracking in the lateral direction. Vecchio and Collins (1982) analyzed the results of their experiments and found that the compressive strength should be reduced as a function of the lateral tensile strain down to 20 %. The large discrepancy between the proposal of Vecchio and Collins and the usual reduction up to 20 %, see for an extensive literature survey Kollegger and Mehlhorn (1990a), was the starting point of a comprehensive experimental study by Kollegger and Mehlhorn at the

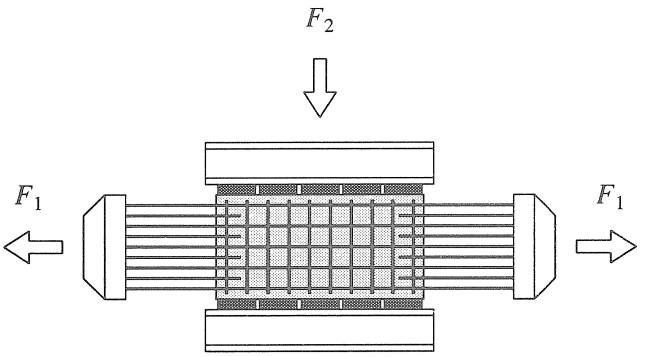

Figure 10 Experiment Kollegger and Mehlhorn (1990a).

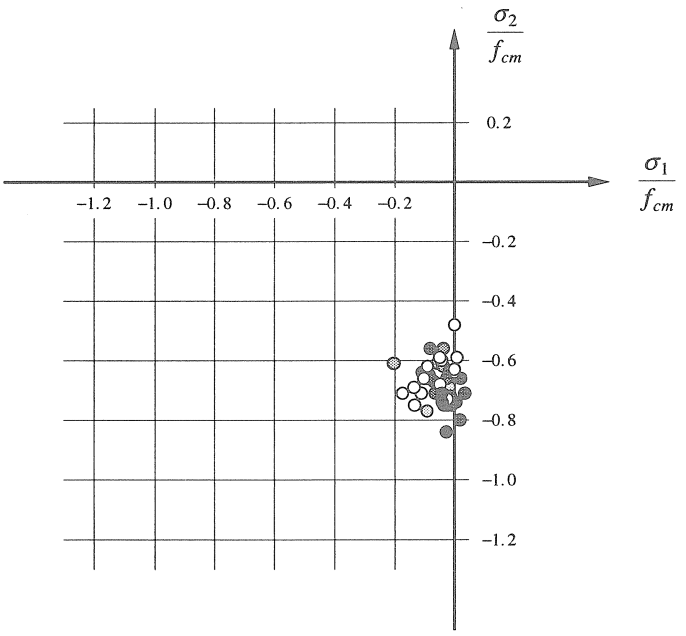

Figure 11 Biaxial strength of reinforced concrete, Kollegger and Mehlhorn (1990a).

University of Kassel. The experimental study concerned 47 panels with dimensions 500×1000 $[mm^2]$ and a thickness of 100 $[mm]$ loaded in a tension-compression state, see Figure 10. The study concerned five series of tests with different reinforcement geometry and reinforcement directions. An influence of the reinforcement properties could not be determined in the study, and a reduction of the compressive strength up to

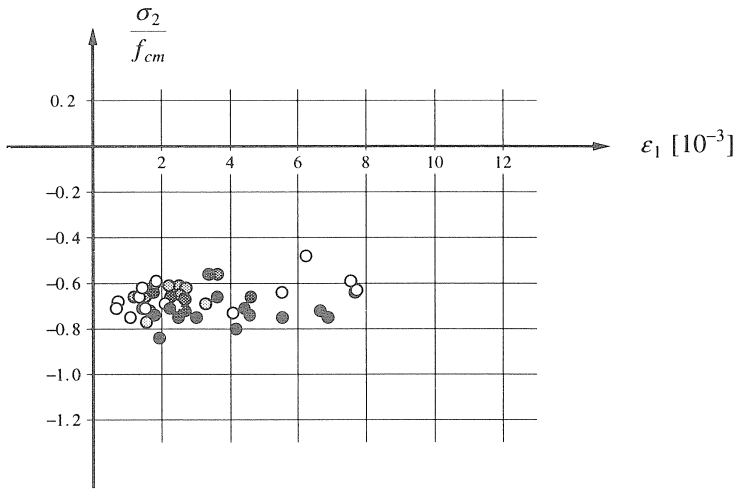

Figure 12 Compressive strength as a function of the transverse strain, Kollegger and Mehlhorn (1990a).

20 % as a function of the transverse tensile stress was proposed. The experimental results of all panels are given in Figure 11 in which the compressive strength of the panels is plotted against the lateral stress. It is clear that the stresses in the panels are compressive in the direction of the tensile loading. These compressive stresses result from prevented lateral strain by the reinforcement in the tensile direction and is calculated by

$$\sigma_1 = \frac{F_1}{A_c} - \sigma_s(\varepsilon_1) \cdot \rho_1$$

with F_1 the tensile force, A_c the concrete area and σ_s the stress in the reinforcement as a function of the strain component ε_1 which is measured on the panel surface. The reinforcement ratio in the lateral direction is denoted by ρ_1. However, when Figure 11 is examined in more detail, it is not obvious that the compressive strength is a function of the transverse stress, since we observe a constant reduction of the compressive strength. If the compressive strength is depicted as a function of the transverse strain, see Figure 12, it is even more obvious that a reduction of the compressive strength as a function of the lateral strain cannot be observed, but that the apparent compressive strength of the panels is approximately 70 % of the mean compressive strength. The compressive strength has been determined with compression tests on concrete cubes $200 \times 200 \times 200$ [mm^3] and the difference between the cube compressive strength and the apparent compressive strength of the panels is according to Kollegger and Mehlhorn the result of the manufacturing of the panels, eccentricities and the nonlinear relation between the mean compressive strength and the biaxial stress state in the panels. The

compressive strength of two panels which have been loaded in compression without tensile loading have been given with a solid dot in Figures 11 and 12. These two panels have been reinforced only by four rebars with a diameter of 6.5 [*mm*] in the corners and also for these two panels a reduction of the compressive strength is observed of approximately 70 %. These panels can be considered as plain concrete and it is obvious that also for these panels the apparent compressive strength is reduced when compared with the cube compressive strength. A possible explanation for this phenomenon is that the compressive strength of concrete is highly influenced by the boundary conditions and the size of the specimen, see Van Mier (1984), Vonk (1992). The size effect and the effect of the boundary conditions should result in a constant reduction of the compressive strength of all panels with or without reinforcement which is indeed observed. Further investigations should give more insight in the mechanisms of strength reduction, size effect and boundary conditions in compressive tests. At present it is assumed that the compressive strength of concrete is reduced by a constant factor of approximately 20 %.

3. Modeling of plain concrete

The mathematical description of material behavior is commonly named a constitutive model. In this study, two different types of constitutive models will be used for the description of plain concrete, firstly constitutive models based on an incremental or a rate formulation, and secondly constitutive models based on a total formulation. The advantages of the first model are that the model allows for a transparent combination with other nonlinear phenomena, such as creep, shrinkage and thermal loading, and that it incorporates path-dependent behavior which allows for non-proportional loading. The advantage of the second model is the conceptual simplicity.

A well established incremental formulation is the fixed multi-directional crack model, De Borst and Nauta (1985), Rots (1988), which allows for a number of non-orthogonal cracks. In this model, a crack is formed perpendicular to the direction of the major principal stress if this stress violates the tensile strength. After the first crack, another crack is allowed to form if the tensile strength is again violated by the major principal stress, and if the angle between the existing crack and the direction of the major principal stress exceeds a certain value, the threshold angle. Usually, this threshold angle is set equal to 30° which implies a maximum number of cracks which are allowed to form of six. However, numerical difficulties have been reported when state changes occur, Crisfield and Wills (1989). To analyze structures which are in a state of compression-tension, e.g. shear wall panels, the crack model can be combined with a plasticity model to describe crack formation and plasticity, De Borst and Nauta (1985), but this combination has been reported to result in numerical difficulties, Wang, Van der

Vorm and Blaauwendraad (1990). Because the major goal of this study is the development of stable numerical tools to analyze reinforced concrete structures, a different model has been formulated to solve both the problem of overestimation of the failure load with the fixed smeared crack model, Rots (1988), and the numerical problems in the tension-compression region. A constitutive model has been developed which describes the formation of cracks within the framework of plasticity. The theory of plasticity is well established and sound numerical algorithms have been developed, see for instance Simo, Kennedy and Govindjee (1988).

The rotating crack model is usually presented in a total strain formulation, see Willam, Pramono and Sture (1986), and this model has been used in the analyses of reinforced concrete structures, Kolleger (1988), Crisfield and Wills (1989). If the Poisson effect is neglected after cracking, the model is probably the most appealing approach for engineers to describe the nonlinear behavior of concrete in tension and compression. A nonlinear compressive behavior is easily implemented in such model, because the algebraic formulation can be extended with a compressive branch. for the rotating crack model.

3.1 Incremental formulation

A constitutive model formulated in an incremental format offers the possibility to model the history of the material implicitly with the definition of internal variables. If an additive decomposition of the strain rate vector $\dot{\boldsymbol{\varepsilon}}$ is assumed into an elastic, reversible part $\dot{\boldsymbol{\varepsilon}}_e$ and an inelastic, irreversible part $\dot{\boldsymbol{\varepsilon}}_c$,

$$\dot{\boldsymbol{\varepsilon}} = \dot{\boldsymbol{\varepsilon}}_e + \dot{\boldsymbol{\varepsilon}}_c \tag{31}$$

the basic formulation is given. The elastic strain rate vector determines the stress rate vector through the elastic stiffness matrix $\boldsymbol{D}_e$

$$\dot{\boldsymbol{\sigma}} = \boldsymbol{D}_e \, \dot{\boldsymbol{\varepsilon}}_e \tag{32}$$

The evolution of the inelastic strain is dependent upon the assumption of the constitutive model and is in general a function of the stress and strain vector and the internal variables. The inelastic strain will now be determined with a incremental formulation based on the flow theory of plasticity. A fundamental notion of plasticity theory is the existence of a yield function

$$f(\boldsymbol{\sigma}, \boldsymbol{q}) = 0 \tag{33}$$

which depends on the stress vector $\boldsymbol{\sigma}$ and on a number of scalar-valued internal variables, conveniently collected in a vector $\boldsymbol{q}$. The inelastic strain vector is now assumed to be given by an associated flow rule,

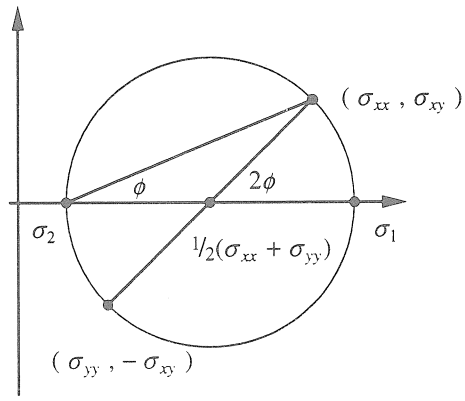

Figure 13 Mohr's circle.

$$\varepsilon_c = \dot{\lambda} \frac{\partial f}{\partial \sigma} \tag{34}$$

with $\dot{\lambda}$ the inelastic multiplier which is determined by the additional constraint that $\dot{f} = 0$.

Consider a plane-stress situation in which the major principal stress σ_1 is defined by means of a Mohr's circle, see Figure 13. The maximum tensile stress criterion of Rankine can then be used to determine the tensile strength of concrete. This results in a yield function which reads

$$f = (\tfrac{1}{2}\sigma^T P_1 \sigma)^{1/2} + \tfrac{1}{2}\pi^T \sigma - \bar{\sigma}(\kappa_T) \tag{35}$$

with the equivalent stress $\bar{\sigma}$ as a function of the internal parameter κ_T. The projection matrix P_1 and the projection vector π are given by

$$P_1 = \begin{bmatrix} 1/2 & -1/2 & 0 & 0 \\ -1/2 & 1/2 & 0 & 0 \\ 0 & 0 & 0 & 0 \\ 0 & 0 & 0 & 2 \end{bmatrix} \tag{36}$$

and

$$\pi = \{ 1 , 1 , 0 , 0 \}^T \tag{37}$$

respectively. The equivalent stress $\bar{\sigma}(\kappa_T)$ is the uniaxial tensile strength which is assumed to be given by one of the tension-softening models given in eq.(13) or eq.(14).

The disadvantage of the Rankine criterion is that the stresses are only bounded in the tensile region. However, the plasticity theory is also applicable to a situation where the

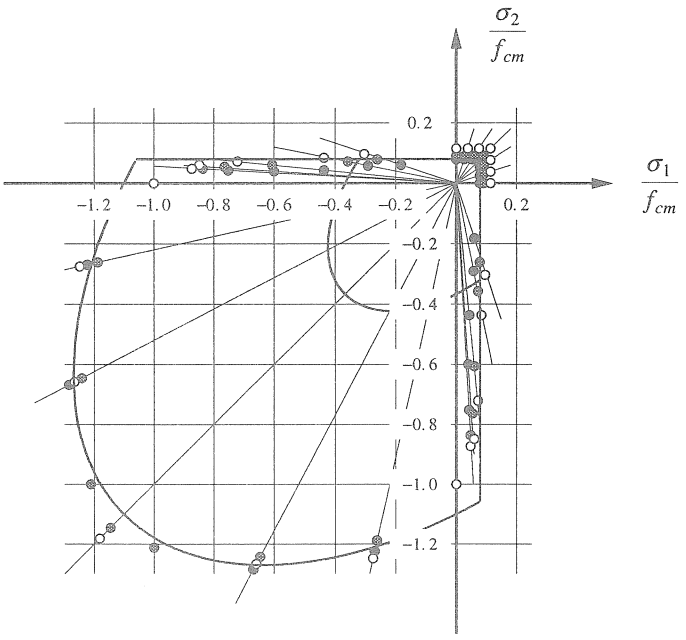

Figure 14 Comparison of a Rankine-Von Mises yield surface with experimental data of Kupfer and Gerstle (1974). $\bar{\sigma}_1 = f_{ct,m}$, $\bar{\sigma}_2 = 1.1\ f_{cm}$

constitutive model consists of two different yield surfaces, one bounding the tensile stresses, the other applicable in the compressive region, which can be represented by

$$\begin{cases} f_1 = 0 \\ f_2 = 0 \end{cases} \tag{38}$$

Comparison with the experimental data of Kupfer and Gerstle (1974) indicates that a composite yield contour can be defined such that a Rankine yield criterion is used to model the tension-tension region and a Von Mises yield function models the compressive stress states, Figure 14. The formulation of the composite yield criterion is given by the function of the Rankine yield function and by the function for the Von Mises yield criterion in the stress space, which results in

$$\begin{cases} f_1 = (\,{}^1\!/_2 \sigma^T P_1\, \sigma\,)^{1/2} + {}^1\!/_2 \pi^T \sigma - \bar{\sigma}_1(\kappa_T) \\ f_2 = (\,{}^1\!/_2 \sigma^T P_2\, \sigma\,)^{1/2} - \bar{\sigma}_2(\kappa_C) \end{cases} \tag{39}$$

with an isotropic hardening rule for both the Rankine and the Von Mises criterion. The Von Mises yield function is determined by the projection matrix

$$P_2 = \begin{bmatrix} 2 & -1 & -1 & 0 \\ -1 & 2 & -1 & 0 \\ -1 & -1 & 2 & 0 \\ 0 & 0 & 0 & 6 \end{bmatrix} \tag{40}$$

and the equivalent stress $\bar{\sigma}_2$ as a function of the internal parameter κ_C. This equivalent stress is the uniaxial compressive strength which is assumed to be given by the parabolic softening model given in eq.(7).

The constitutive model is now given by a composite yield surface which bounds the stresses in the tension-tension, tension-compression and the compression-compression regions. The material behavior, as described in Chapter 2, is determined by tthe internal parameters, κ_T and κ_C. For details about the numerical elaboration the reader is referred to Feenstra (1993).

3.2 Total formulations

The fundamental difference between the total formulation of the constitutive model and the incremental formulation discussed in the previous paragraphs is the formulation in strains rather than in strain rates. Commonly used total formulations are the fixed and rotating crack models, Willam, Pramono and Sture (1986), Rots (1988), Crisfield and Wills (1989). In this study the elasticity-based rotating crack model in a co-rotational format is used with the assumption that the local constitutive model which describes the relation between the local stress vector and the local strain vector, is transformed into the global coordinate system with a transformation matrix which is determined by the principal directions of the strain vector. The strain vector in the global coordinate system $\boldsymbol{\varepsilon}$ is updated by the incremental strain vector which follows from the equilibrium iterations, according to

$$\boldsymbol{\varepsilon} = \boldsymbol{\varepsilon} + \Delta\boldsymbol{\varepsilon} \tag{41}$$

which is transformed to the strain vector in the local coordinate system $\boldsymbol{\varepsilon}_{n,s}$ with the strain transformation matrix $\boldsymbol{T}(\phi)$

$$\boldsymbol{\varepsilon}_{n,s} = \boldsymbol{T}(\phi)\, \boldsymbol{\varepsilon} \tag{42}$$

with

$$T(\phi) = \begin{bmatrix} \cos^2\phi & \sin^2\phi & 0 & \sin\phi\cos\phi \\ \sin^2\phi & \cos^2\phi & 0 & -\sin\phi\cos\phi \\ 0 & 0 & 1 & 0 \\ -2\sin\phi\cos\phi & 2\sin\phi\cos\phi & 0 & \cos^2\phi - \sin^2\phi \end{bmatrix}$$

The constitutive model has to be formulated in the local coordinate system and should give a relation between the local strain vector $\boldsymbol{\varepsilon}_{n,s}$ and the local stress vector $\boldsymbol{\sigma}_{n,s}$. In an unconstrained stress situation the general format reads

$$\boldsymbol{\sigma}_{n,s} = \boldsymbol{D}(\boldsymbol{\varepsilon}_{n,s})\, \boldsymbol{\varepsilon}_{n,s} \tag{43}$$

The updated stress vector in the global coordinate system is then given by

$$\boldsymbol{\sigma} = \boldsymbol{T}(\phi)^T \boldsymbol{\sigma}_{n,s} \tag{44}$$

This general formulation does not necessarily maintain co-axiality, because the principal axes of stress do not need to coincide with the principal axes of strain. The formulation presented here is merely a framework for the treatment of the rotating and the fixed crack models within a total strain formulation, in order to compare the incremental and total approaches. For more details see Feenstra (1993).

3.3 Tension-shear model problem

The fundamental differences of the formulations discussed in this chapter will be discussed with an elementary problem proposed by Willam, Pramono and Sture (1986), in which a plane-stress element with unit dimensions is loaded in biaxial tension and shear. This causes a continuous rotation of the principal strain axes after cracking, as is typical of crack propagation in smeared crack finite element analysis. The element is subjected to tensile straining in the x-direction accompanied by lateral Poisson contraction in the y-direction to simulate uniaxial loading. Immediately after the tensile strength has been violated, the element is loaded in combined biaxial tension and shear strain, see Figure 15. The ratio between the different strain components is given by $\Delta\varepsilon_{xx} : \Delta\varepsilon_{yy} : \Delta\gamma_{xy} = 0.5 : 0.75 : 1$. The material properties are given in Table 2. The analyses of Rots (1988) of this problem with the multi-directional crack model show that the shear response becomes softer with decreasing threshold angle, resulting in the limiting case of the rotating crack model with zero threshold angle as the most flexible response.

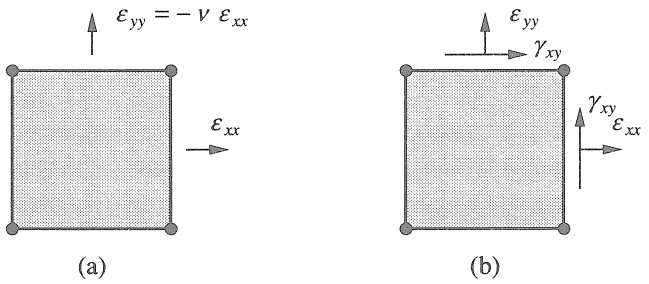

Figure 15 Tension - shear model problem: (a) tension up to cracking; (b) biaxial tension with shear beyond cracking.

Table 2 Material properties tension-shear model problem.

	concrete	
E_c	10000	$[N/mm^2]$
ν	0.2	[–]
$f_{ct,m}$	1.0	$[N/mm^2]$
G_f	$0.15\ 10^{-3}$ 1)	$[Nmm/mm^2]$

1) linear softening

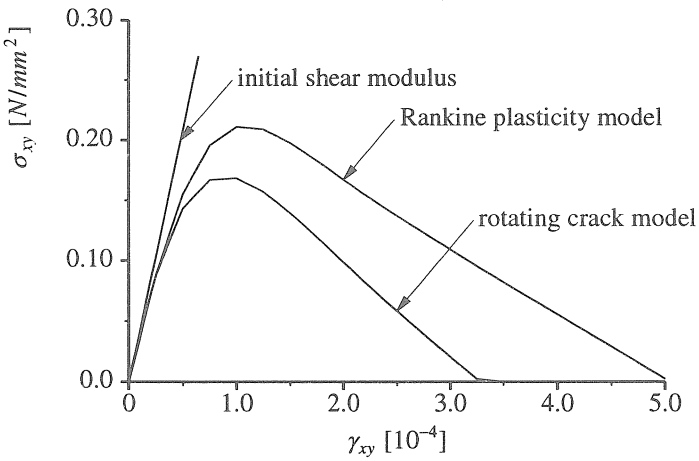

Figure 16 $G_f = \infty$. $\sigma_{xy} - \gamma_{xy}$ response.

The behavior of the different formulations for smeared cracking which have been given can be studied in detail with this problem. The constitutive behavior will be

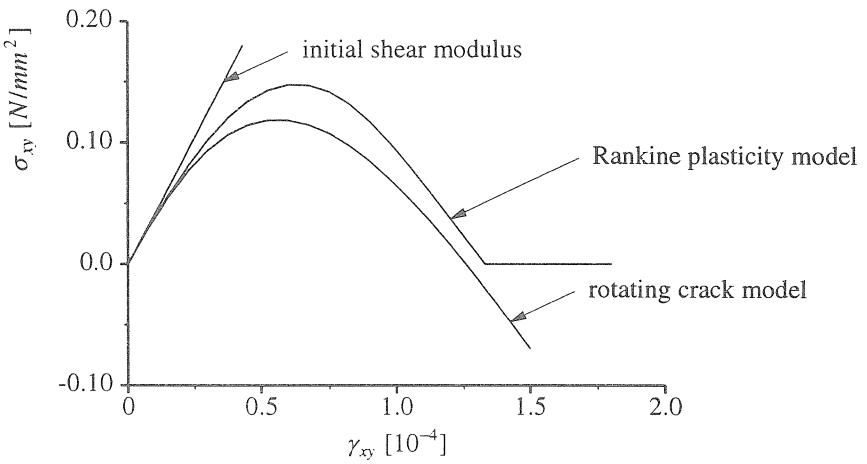

Figure 17 Rankine plasticity model and the rotating crack model. $\sigma_{xy} - \gamma_{xy}$ response.

compared with respect to the shear stress - shear strain behavior and the normal stress - normal strain behavior in the x- and y-directions. Particularly the shear stress - shear strain response gives a good impression of the behavior of the model when applied to the analyses of structures.

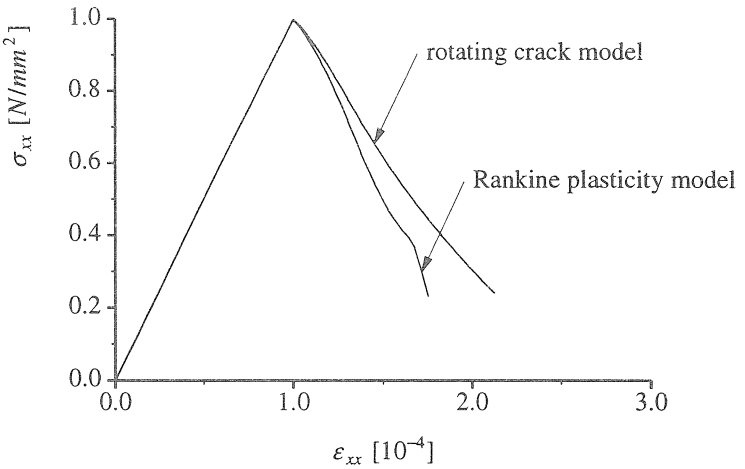

Figure 18 Rankine plasticity model and the rotating crack model. $\sigma_{xx} - \varepsilon_{xx}$ response.

The second issue is the comparison of the rotating crack model and the Rankine plasticity model within an incremental formulation. Because the response of models with a total formulation is in general more flexible than the response of models with an

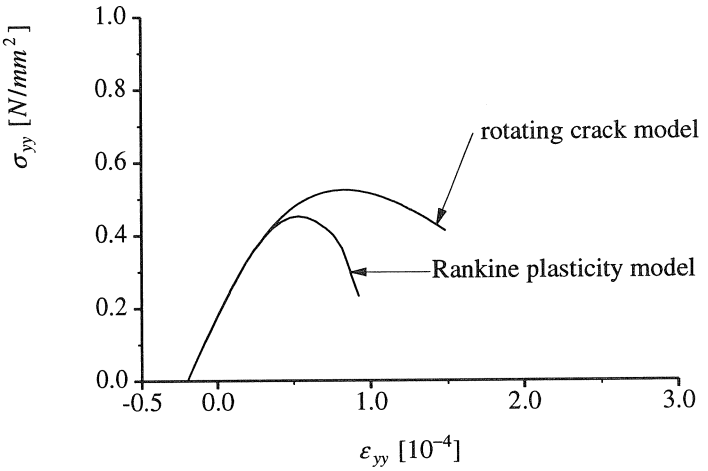

Figure 19 Rankine plasticity model and the rotating crack model. $\sigma_{yy} - \varepsilon_{yy}$ response.

incremental formulation, we expect that the Rankine plasticity model with an incremental formulation shows a less flexible shear stress - shear strain response, but the comparison should provide insight if this less flexible response is still acceptable.

The limiting case with no softening ($G_f = \infty$) confirms that the formulation within the total strain concept results in a more flexible response than the incremental formulation. The shear stress-shear strain responses of the rotating crack model and the Rankine plasticity model are shown in Figure 16. It is clear from this figure that although no softening has been assumed, the shear stress-shear strain response shows an implicit softening behavior.

The plasticity model based on an incremental formulation has also been applied to the tension-shear model problem with the material properties given in Table 2 and compared with the rotating crack model in the following figures. The first interest concerns the behavior in shear which is depicted in Figure 17. It is clear from this figure that the rotating crack model has the most flexible response in shear, but the differences between the rotating crack model and the Rankine plasticity model are minor. The Rankine plasticity model results in a shear stress equal to zero when the apex of the yield surface has been reached. The normal stress-strain response in the x-direction, see Figure 18, shows an implicit normal stress-shear stress coupling for the models with an even more pronounced coupling for the Rankine plasticity model. The normal stress-normal strain response in the lateral direction, depicted in Figure 19 shows the linear softening relation when the apex of the yield surface has been reached.

4. Application to plain concrete

The objective of this chapter is to compare the Rankine plasticity model and the rotating crack model in applications to plain concrete structures. It will be shown that the Rankine plasticity model is well capable to simulate crack propagation in plain concrete.

4.1 Single-edge-notched beam

The single-edge-notched geometry of the Iosipescu beam has been used in experiments on concrete beams for the first time by Arrea and Ingraffea (1982). The experiments show a curved crack propagating from the tip of the notched to the opposite side of the loading platen. The experiments on the SEN-specimen have been simulated extensively during the last decade, see De Borst (1986), Rots (1988), Rots (1992), Schlangen (1993). RILEM committee 89-FMT has also proposed an experimental round robin using the SEN-specimen to study the mixed-mode fracture process. The proposed experimental set-up has been improved such that the experiments could be performed without friction in the roller bearings, see for more details Schlangen (1993). The scatter of the experimental results is small which makes the experiments very suitable for numerical simulation. The stress state in the specimen is mainly tension-shear with small compressive stresses. The objective of the analyses presented here is to simulate curved mode I fracture propagation with the rotating crack model and the Rankine plasticity model with an incremental formulation.

Table 3 Material properties single-edge-notched beam.

	concrete	
f_{cm}	36.5	$[N/mm^2]$
E_c	35000	$[N/mm^2]$
ν	0.15	[–]
$f_{ct,m}$	2.8	$[N/mm^2]$
G_f	0.07[1)]	$[Nmm/mm^2]$

1) exponential softening

The SEN-specimen are $400 \times 100 \times 100$ $[mm^3]$ with a notch of 5×20 $[mm^2]$. The distance between the inner supports is equal to 40 $[mm]$ and the distance between the outer supports is equal to 400 $[mm]$. The specimen has been discretized with 1655 three-noded plane-stress elements with a single integration point and a very dense distribution of elements around the tip of the notch, see Figure 20. The distribution of the loads has been modeled as described by Schlangen (1993), with $F_1 = 10/11\ F$ at the center loading platen and $F_2 = 1/11\ F$ at the outer loading platen, with F the total load. Only the center loading platen has been modeled because only this platen has an influence on the stress distribution. The middle support has been fixed in the vertical

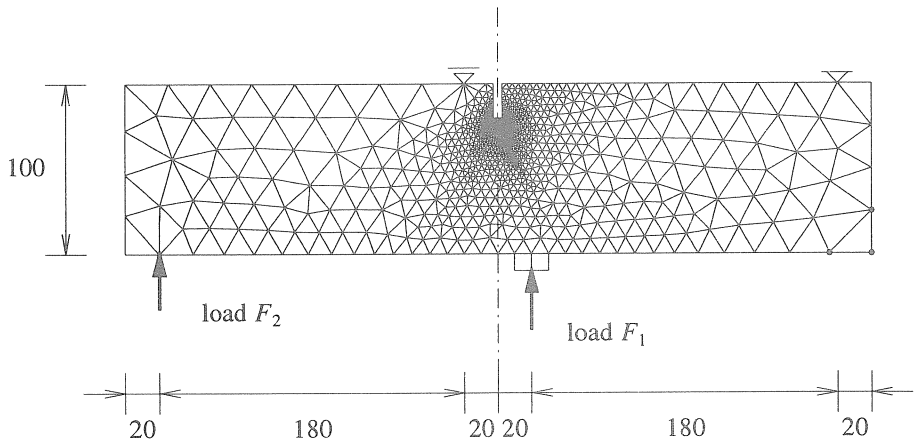

Figure 20 Single-edge-notched beam. Finite element mesh. Measures in [*mm*].

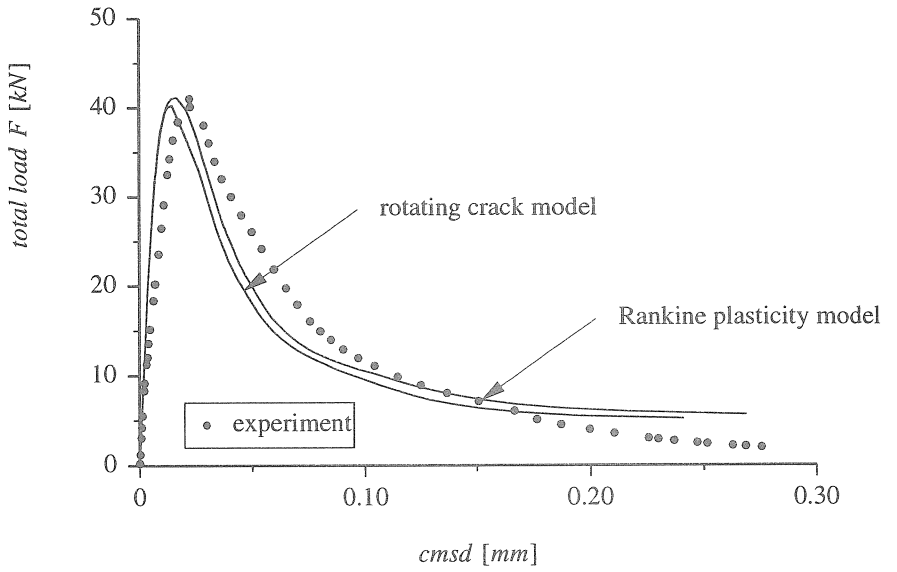

Figure 21 Single-edge-notched beam. Load-cmsd diagram.

direction and the outer support has been fixed in vertical and horizontal directions. The experiments on the small beams with normal weight concrete, maximum aggregate 8 [*mm*], have been chosen for the numerical simulation, with the material properties given in Table 3. The analyses have been performed using an advanced solution technique with a full Newton-Raphson iteration method with an automatic load stepping

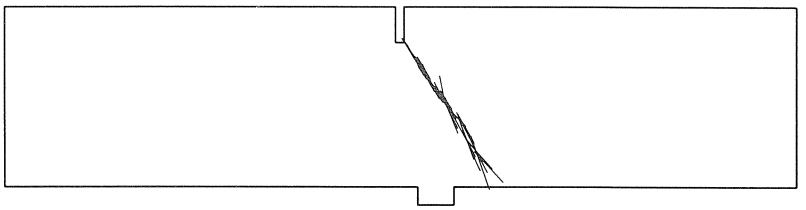

Figure 22 Single-edge-notched beam. Active cracks at final load.

scheme based on external work. The iteration method has been enhanced using a line search technique. For more details regarding the solution technique, see Feenstra (1993). The convergence characteristics of the calculations are good, although for the rotating crack model a number of line searches were necessary. The comparison of the experimental result and the numerical simulations focuses on the crack-mouth-sliding-displacement (cmsd) versus the total load which should be considered as a representative measure of the nonlinear behavior of the structure. The total load-cmsd diagram, Figure 21, shows a pre-peak behavior which is a little too stiff for all models and a failure load which is in accordance with the experimental result. The post-peak behavior is simulated within acceptable boundaries for all models. It appears that the different formulations of the constitutive models do not differ very much. Neither of the models is capable to predict a genuine separation with a full softening behavior which has been found in the experiment. An analysis with a discrete crack model, Rots (1988), of a similar beam shows a full softening behavior, but the analyses with other smeared crack models show the same tendency. At peak load the crack has been initiated at the right-hand-side of the notch with a direction of approximately 45° which has also been observed in the experiments, Schlangen (1993). At the final load the crack is propagated through the specimen from the notch to the right-hand-side of the loading platen which is shown in Figure 22 for the analysis with the Rankine model. Only the active cracks have been plotted which are defined as the integration points which have an internal parameter which is larger or equal to $0.5\ \kappa_u$, with κ_u defined in eq.(15). The crack pattern of the analysis with the rotating crack model is almost equal to the crack pattern of the Rankine plasticity model. The differences between the models are small and only perceptible in the final load stage.

4.2 Pull-out of an anchor bolt

The pull-out analysis of an anchor bolt has been proposed by RILEM-committee TC90-FMA as a round-robin analysis in order to compare the different analytical and numerical methods. The geometry and material properties of the first proposal for the round-robin, Elfgren (1990), have been used to simulate the pull-out with the standard

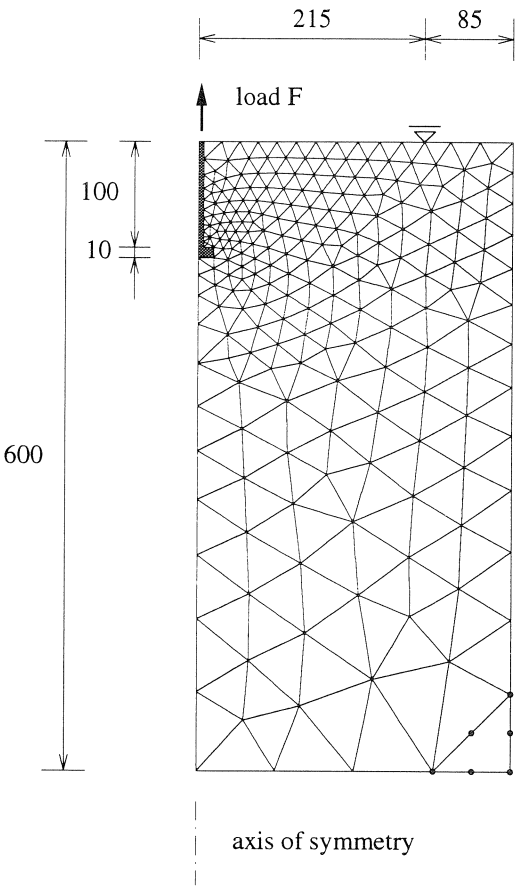

Figure 23 Pull-out of an anchor bolt. Finite element model. Measures in [*mm*].

smeared crack models for both the plane-stress and the axisymmetrical case, Feenstra, Rots and De Borst (1990). The second, revised invitation also concerned the experimental analysis of the proposed geometry for both the plane-stress and axisymmetrical case with an embedded depth of 50, 150 and 450 [*mm*] respectively. In the Stevin Laboratory at Delft University of Technology experiments have been carried out on a plane-stress specimen with an embedded depth of 100 [*mm*], Vervuurt, Schlangen and Van Mier (1993). These experiments have been used in this study to investigate the behavior of the Rankine plasticity model and the rotating crack model.

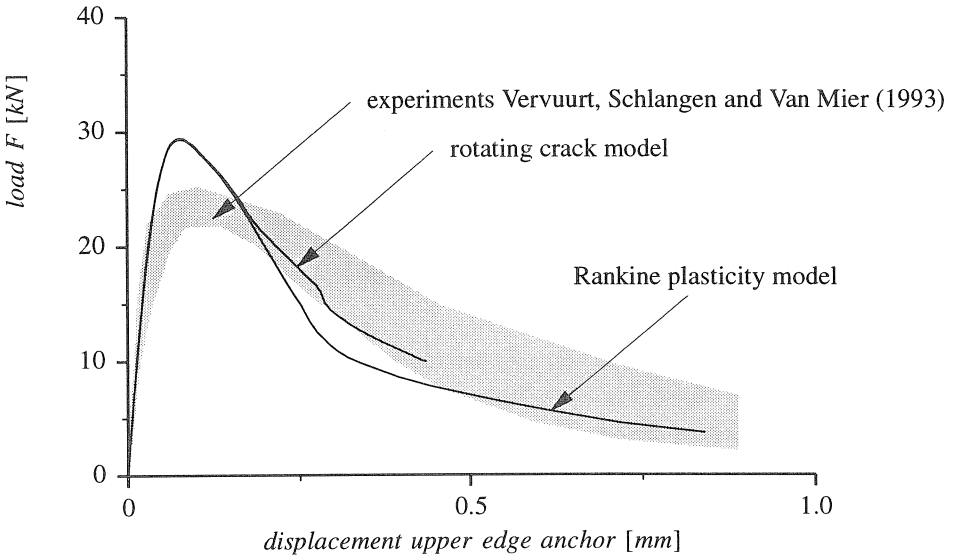

Figure 24 Pull-out of an anchor bolt. Load - displacement diagram.

Table 4 Material properties pull-out of an anchor bolt.

	concrete	
f_{cm}	35.0	$[N/mm^2]$
E_c	37000	$[N/mm^2]$
ν	0.15	[–]
$f_{ct,m}$	2.5	$[N/mm^2]$
G_f	0.09[1)]	$[Nmm/mm^2]$
G_c	5.0[2)]	$[Nmm/mm^2]$

1) exponential softening
2) parabolic softening

The finite element discretization is given in Figure 23. Only half of the specimen has been discretized with 402 six-noded plane-stress triangles with a seven-point integration. The anchor has been modeled using 13 four-noded plane-stress elements with a four-point integration. The material properties are given in Table 4.

The results are given as the load versus the displacement of the upper-outer edge of the anchor head and the crack pattern at different stages of the calculation. The load displacement diagram is given in Figure 24 for the different constitutive models. Analyses with the composite yield surface show that the influence of the compressive nonlinearity on the load-displacement curve is negligible and these diagrams are not shown in Figure 24. The predicted failure load is approximately 20 % too high when compared

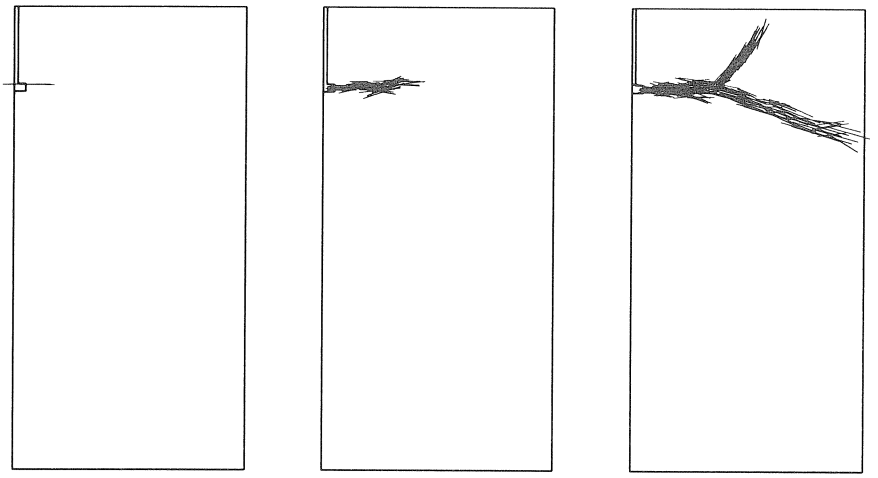

(a) (b) (c)

Figure 25 Pullout of an anchor bolt. Active cracks (a) just before maximum load ; (b) just after maximum load ; (c) final crack pattern

with the experimental results, but the post-peak behavior is predicted in agreement with the experimental response. It is remarkable that the failure load is almost equal for both constitutive models but that the post-peak behavior shows substantial differences. The rotating crack model results in a load-displacement diagram which is less brittle than the Rankine plasticity model. The calculations of the rotating crack model have been terminated at an early stage because convergence could no longer be achieved. The failure mode is a sudden crack propagation which is clearly shown by the crack pattern of the Rankine plasticity model is shown in Figure 25. Just before the maximum load the cracks localize in a small region around the anchor head and after the maximum load the crack propagates horizontally through the specimen which is accompanied with a decreasing load. When the crack has grown towards the support it branches into two cracks, one propagating in the direction of the support, and one propagating downwards. This crack branching has also been observed in the experiments where it is even more pronounced because the crack pattern in the specimen is nonsymmetric, see Vervuurt, Schlangen and Van Mier (1993). The crack propagating downwards is the active crack which can be seen from the displacements plotted in Figure 26 for three different load stages. This analysis shows that the constitutive models which have been developed are capable to predict the failure load, the post-peak behavior and the failure mode accurate enough to be used in the analysis of a design problem which is formulated by RILEM-committee TC90-FMA as one of the goals.

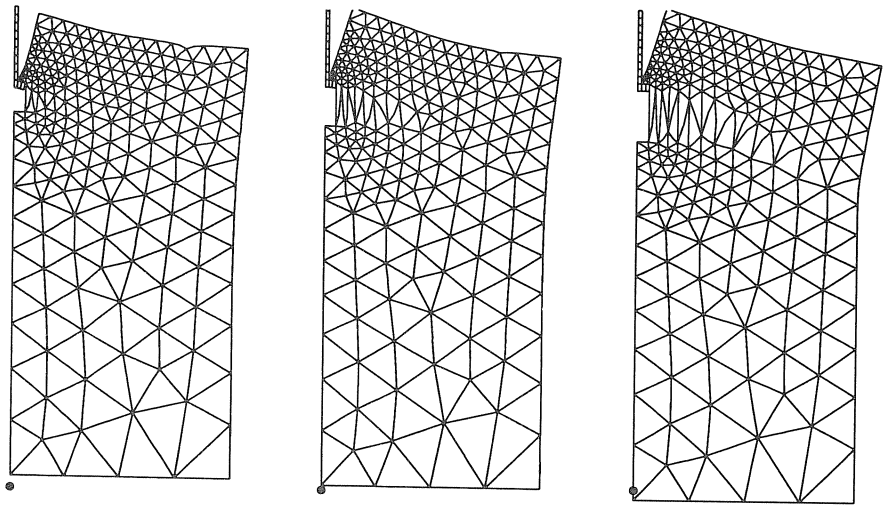

(a) (b) (c)

Figure 26 Pullout of an anchor bolt. Total displacements. (a) just before maximum load ; (b) just after maximum load ; (c) at final load.

4.3 Cylinder splitting test

The cylinder splitting test is often used as an indirect test for determining the tensile strength of concrete. However, the tensile strength which can be derived from this test is considerably influenced by the boundary conditions and failure is often induced by compressive softening under the loading platen, see Hannant, Buckley and Croft (1973). Although the stress state under the loading platen is considered to be triaxial, this example has been chosen to analyze the capability of the developed models to predict the failure mode in a tension-compression test. The geometry of the cylinder splitting test has been taken from a similar analysis of Saourides and Mazars (1989) who analyzed this example with a local and nonlocal damage model. Their conclusion was that it is not possible to obtain a splitting type of failure with a traditional local approach because damage localizes under the loading area. The fracture-energy based models which will be used in this study may provide a solution as will be shown in the following analysis.

The specimen which will be analyzed is a cylinder with a length of 160 [*mm*] and a cylinder radius of 40 [*mm*]. Only a quarter of the specimen is discretized because of symmetry conditions, with 105 six-noded plane-stress elements with a 7-point integration. The loading platen has been modeled with one 8-noded plane-stress element with a 9-point integration. The finite element discretization is shown in Figure 27 and the material properties which have been used are given in Table 5.

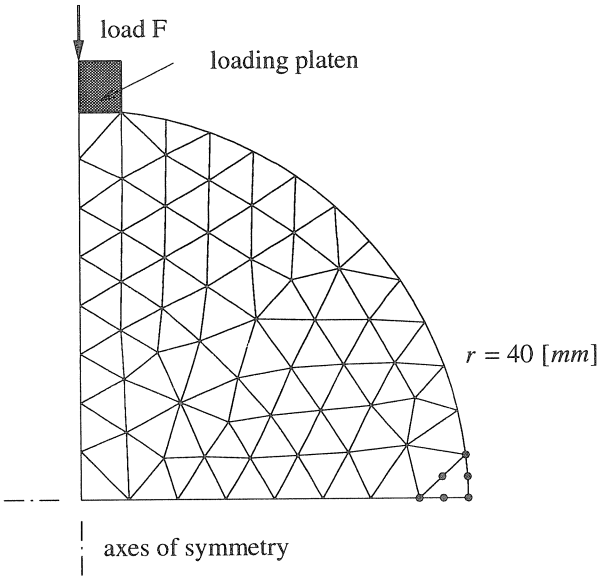

Figure 27 Cylinder splitting test. Finite element mesh.

Table 5 Material properties cylinder splitting test.

	concrete	
f_{cm}	30.0	$[N/mm^2]$
E_c	37700	$[N/mm^2]$
ν	0.15	[–]
$f_{ct,m}$	3.0	$[N/mm^2]$
G_f	0.10[1)]	$[Nmm/mm^2]$
G_c	5.0[2)]	$[Nmm/mm^2]$

1) exponential softening
2) parabolic softening

The load versus the displacement of the loading platen is depicted in Figure 28 in which the influence of the compression softening is clearly shown. If no compression softening is modeled, the analysis does not resuls in a limit load, but gives a monotonically increasing load displacement curve. The differences between the Rankine plasticity model and the rotating crack model are negligible which is not surprising because the crack can be considered as a pure mode-I crack which does not rotate after cracking.

If compression softening is taken into account the situation changes considerably. The ultimate load is smaller than the ultimate load of the composite yield function because of the different failure mechanism. The failure mechanism of the rotating crack model is completely governed by compression softening. On the other hand, a splitting crack is observed for the composite yield function. The biaxial stress state under the

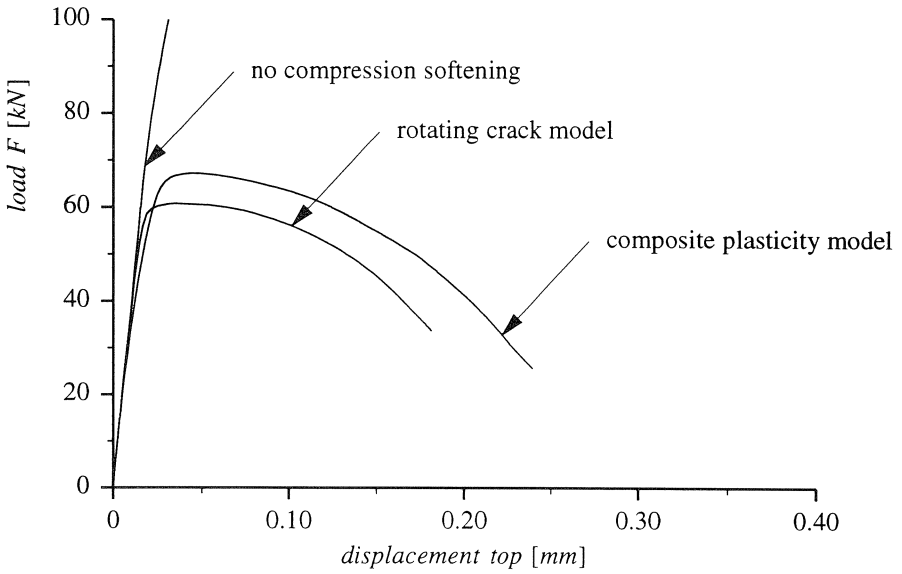

Figure 28 Cylinder splitting test. Load - displacement diagram.

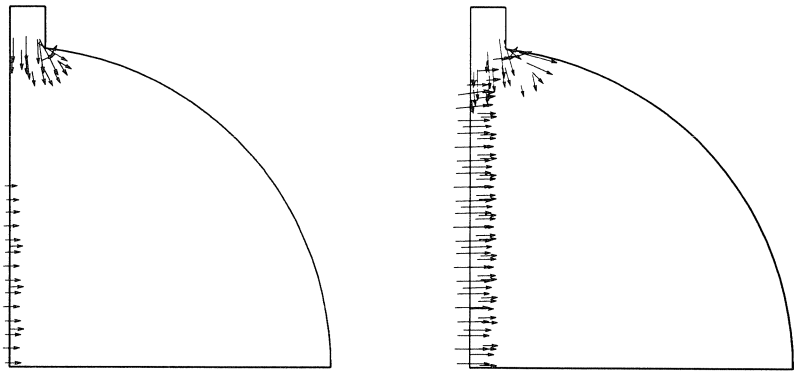

Figure 29 Cylinder splitting test. Principal plastic strain. (a) at maximum load ; (b) at final load.

loading platen is clearly shown by the principal inelastic strain vectors which are plotted in Figure 29 at the maximum load and at the final state. At the maximum load the stress state under the loading platen is mainly mode-I compression with a starting splitting crack in the middle of the specimen. This crack propagates in the vertical direction

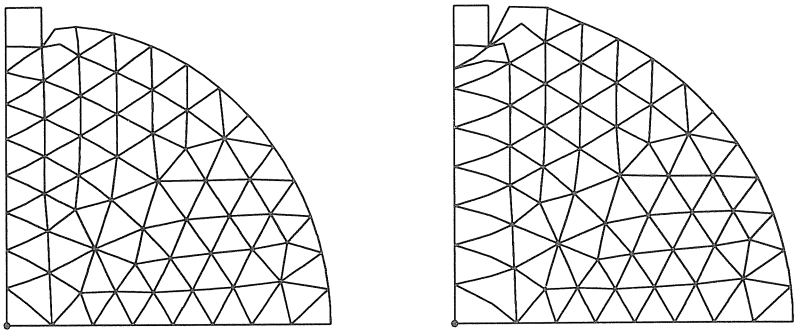

(a) (b)

Figure 30 Cylinder splitting test. Total displacements. (a) at maximum load ; (b) at final load.

which is attended by a descending load-displacement curve. The total displacements of the specimen, depicted in Figure 30, show clearly the crack in the middle of the specimen and the inelastic deformations under the loading platen. It is clear that the constitutive model which is used to analyze the cylinder splitting test is of utmost importance for the calculated response. If the nonlinear behavior due to compression softening is neglected, no limit load will be found, cf. Labbane, Saha and Ting (1993).

5. Modeling of reinforced concrete

The modeling of reinforcement in a finite element method is possible via three ways which have been used extensively during the last decades. A distributed representation of the reinforcement is probably the most frequently used method. In this approach the reinforcement is assumed to be distributed over the concrete element with a particular orientation angle. In slabs and shells, but also in panels, this method is implemented in a layered element where some layers represent the reinforcement and it is assumed that a state of plane-stress exists in each layer. An embedded formulation is often used in connection with iso-parametric elements, such that the displacements of the reinforcing bars or grids are the same as the displacement of the parent-element. Finally, a discrete representation of reinforcement is also possible. Uniaxial elements are superimposed to the elements representing the concrete with rigid connections or with interface elements. With the latter approach, bond slip between the concrete and the reinforcement can be modeled explicitly. In the first two approaches it is generally assumed that perfect bond

exists between concrete and reinforcement. In this study, an embedded formulation of reinforcement will be used with the assumption of perfect bond between concrete and reinforcement.

The reinforcement in concrete structures is usually applied in differently orientated layers of reinforcing grids. Because of the one-dimensional character of these grids, it is generally not necessary to introduce multiaxial constitutive models for the reinforcing steel, Chen (1982), and the experimental stress-strain curve for axial loading is idealized as a uniaxial elasto-plastic constitutive model with work-hardening. The behavior in compression and tension is considered to be equal because buckling under compressive forces is prevented by the concrete cover.

5.1 Constitutive model of reinforced concrete

The behavior of reinforced concrete loaded in tension has been considered as the superposition of a material model for plain concrete, a material model for reinforcement and an additional stiffness which is referred to as the tension-stiffening component. The constitutive model for plain concrete, discussed in Chapter 3, has been derived as a fracture energy-based tension-softening model. The amount of fracture energy of a single crack has been assumed to be dissipated over an equivalent length which is related to the element size. In reinforced concrete usually a number of cracks develop during the process of loading until the cracking process stabilizes and no further cracks develop in the structure. The crack spacing at stabilized cracking is determined mainly by the amount of reinforcement. It is assumed in this study that the material model for plain concrete, based on fracture energy, can be applied to reinforced concrete with the total amount of fracture energy dissipated over the equivalent length. Because the fracture energy is assumed to be a material parameter, only the average crack spacing has to be determined, see Chapter 2.

The constitutive model of the reinforcement is assumed to be given by an elasto-plastic model with a linear-elastic stiffness matrix given by

$$\boldsymbol{D}_e^r = \begin{bmatrix} \rho_p E_s & 0 & 0 \\ 0 & \rho_q E_s & 0 \\ 0 & 0 & 0 \end{bmatrix} \tag{45}$$

in which ρ_p and ρ_q the reinforcement ratio in the p- and q-direction respectively and E_s the Young's modulus of the reinforcement. The shear stiffness of the reinforcing grid is assumed to be equal to zero.

In general, bond is assumed between reinforcement and concrete which is of fundamental importance for the constitutive model of reinforced concrete. Due to the bond action a series of cracks will develop in a reinforced member subjected to a tensile loading. The average crack spacing is in general a function of the amount and distribution of the reinforcement, concrete cover on the reinforcement and the tensile strength of the

concrete. At a certain load stage the crack spacing will stabilize and a subsequent increase of the load no longer results in additional cracking. It is observed that also after stabilized cracking, the cracked reinforced concrete is still capable to carry stresses between two adjacent cracks which increases the overall stiffness of the structure. This phenomenon is called tension-stiffening and is related to the direction and properties of the reinforcement. In this study, the additional stiffness will be modeled with a constitutive model which describes the additional stiffness as a function of the strain in the direction of the reinforcement as discussed in Chapter 2 with a stiffness matrix given by

$$D_{ia}^{r} = \begin{bmatrix} E_{b,p} & 0 & 0 \\ 0 & E_{b,q} & 0 \\ 0 & 0 & 0 \end{bmatrix} \tag{46}$$

in which $E_{b,p}$ and $E_{b,q}$ the bond stiffness in the p- and q-direction of the grid respectively. The constitutive model for tension-stiffening is in general a function of the reinforcement ratio, the diameter of the reinforcement and the average crack spacing.

The shear resistance of cracked reinforced concrete is determined by a combination of aggregate interlock, dowel action and the axial restraint stiffness of the reinforcement crossing a crack, see Walraven and Reinhardt (1981), Gambarova (1987), Vecchio and Nieto (1991). The resulting shear stress-shear strain response of aggregate interlock and dowel action shows a similar behavior, but in general it is assumed that aggregate interlock dominates over dowel action at small crack widths. The aggregate interlock models generally result in quite complex formulations even if the models are implemented in interface elements in which the constitutive relations are described in terms of crack opening and crack sliding, see e.g Feenstra, de Borst and Rots (1991a, 1991b). Implementation in a smeared approach, in which average strains and stresses are considered, is not readily possible because a simple, mathematical model defined in terms of the strain vector is not available. It is therefore assumed that the shear stiffness of the interaction model is equal to zero.

As discussed in Chapter 2, the constitutive model of cracked reinforced concrete will be given by the superposition of the constitutive models of the plain concrete, the reinforcement and the interaction between concrete and reinforcement. In this manner, we have a phenomenological description of the material behavior of a composite material by describing the material models of the constituent materials and their mutual interaction in a separate manner.

5.2 Constitutive model for plain concrete

The constitutive model for plain concrete has been discussed in Chapter 3. It has been shown that in applications to plain concrete the Rankine plasticity model gives good results, see Chapter 4. The constitutive model for the tension-softening component of reinforced concrete is again assumed to be given by either the incremental or the total

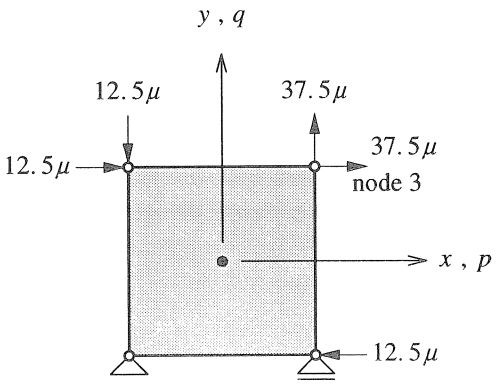

Figure 31 Idealized reinforced panel. Finite element configuration.

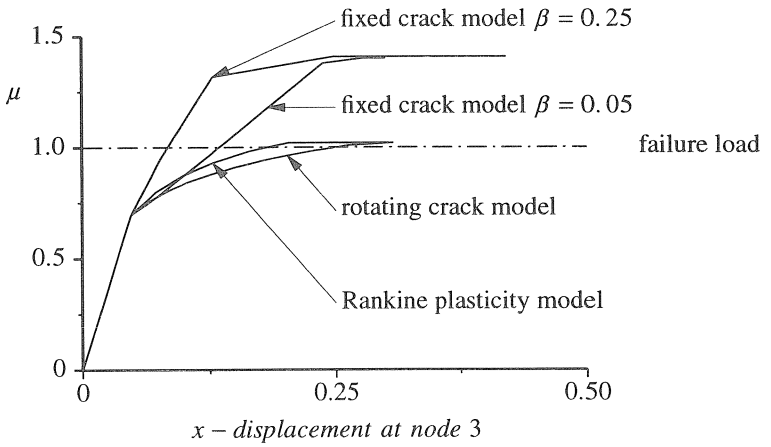

Figure 32 Idealized reinforced panel. Comparison of different concrete models.

formulation. The constitutive models have been applied to an idealized panel proposed by Crisfield and Wills (1989) in order to determine whether the same conclusion can be drawn regarding the constitutive model of plain concrete. The analysis concerns a single element, dimensions 10×10 $[mm^2]$ with a thickness of 1 $[mm]$, reinforced with one layer of a reinforcing grid. The finite element configuration is shown in Figure 31. The reinforcement ratio in the p-direction is equal to 0.04232 and equal to 0.00768 in the q-direction. The analysis is a no-tension analysis with linear-elastic behavior in compression which results in a limit analysis with the exact failure load. The material properties are given in Table 6.

Table 6 Material properties idealized panel.

concrete		
E_c	20000	$[N/mm^2]$
ν	0.0	[–]
$f_{ct,m}$	0.0	$[N/mm^2]$
G_f	0.0	$[Nmm/mm^2]$
reinforcement		
f_{sy}	500	$[N/mm^2]$
E_s	200000	$[N/mm^2]$

The panel is loaded in a combined biaxial tension-shear loading with $f_{xx} = f_{yy} = 2.5\mu$ $[N/mm^2]$ and $f_{xy} = 5.0\mu$ $[N/mm^2]$ with μ the loading parameter which is equal to one for the exact collapse load which is associated with yielding of the reinforcement. The results of the analyses is shown in Figure 32, where the loading parameter is plotted against the x-displacement of the upper-right node of the element. The comparison of the different formulations of the constitutive model for plain concrete shows that the formulation is important even if the tensile strength is equal to zero and no tension-softening description is used. The interaction between the reinforcement and the concrete compressive struts after cracking results in different responses. The fixed crack model shows a collapse load which is too high, irrespective of the magnitude of the shear retention factor β. The rotating crack model and the Rankine plasticity model approximate the exact failure load closely.

The choice of the constitutive model for plain concrete can be based on the fundamental difference which has been shown with this example. If the fixed crack model is adopted, the failure load will often be too high which has also been shown before by Crisfield and Wills (1989) with the analyses of seven reinforced concrete panels tested by Vecchio and Collins (1982). The rotating crack model on the other hand gives failure loads which are in better agreement with the experimentally observed collapse loads. A deficiency of a total formulation, like the rotating crack model, is that a transparent combination with other nonlinear phenomena is often difficult and an incremental formulation is therefore preferred. The Rankine plasticity model with an incremental formulation shows a behavior which is quite similar to the behavior of the rotating crack model and can be used to model plain concrete. Because the Rankine plasticity model has shown to be accurate and results in stable numerical computations, this model will be used in the remainder of this study.

5.3 Validation of the tension-stiffening model

The tension-stiffening effect is usually referred to in the literature as the ability to gradually redistribute the load in a structure from concrete to steel under the formation of primary and secondary cracks. In this study however, the tension-stiffening effect is only used to define the additional stiffness due to the interaction between concrete and reinforcement whereas the formation of primary and secondary cracks has been modeled with the constitutive model of plain concrete, the tension-softening model.

The tension-stiffening model has been validated with experiments on reinforced concrete panels subjected to in-plane shear and normal loading. The loading regime and the properties of the reinforcement of the experiments are designed such that no rotation of the principal strain occurs after cracking. Only the model which describes the tension-stiffening effect is utilized and dowel action is not activated. The panels are 890×890 $[mm^2]$ with a thickness of 70 $[mm]$, reinforced with two layers of a reinforcing grid. The cover of the reinforcing grids is equal to 6 $[mm]$ for all panels which have been analyzed. The finite element idealization for the analyses consists of a four-noded element with four integration points for both the reinforcement and the concrete. The reinforcement in the panels is represented by the angle ψ between element x-axis and main reinforcement p-axis and the reinforcement ratios in p- and q-directions.

The tension-softening of the concrete has been applied with a linear diagram and the additional stress due to the tension-stiffening effect has been applied with the diagram given in chapter 2.

The first analyses concern the panels of Bhide and Collins (1987) who tested a series of thirty-one, uniaxially reinforced concrete panels subjected to various combinations of tension and shear. For the validation of the tension-stiffening model two panels, panels pb13 and panel pb25, have been selected. Both panels have approximately the same material properties, but the reinforcement ratio of panel pb25 is twice the reinforcement ratio of panel pb13. The panels are both loaded in uniaxial tension in the direction of the reinforcement.

Table 7 Material properties panel pb13.

concrete		
f_{cm}	23.4	$[N/mm^2]$
E_c	26000	$[N/mm^2]$
ν	0.15	[–]
$f_{ct,m}$	1.85	$[N/mm^2]$
G_f	0.06[1)]	$[Nmm/mm^2]$
reinforcement		
f_{sy}	414	$[N/mm^2]$
E_s	210000	$[N/mm^2]$

1) linear softening

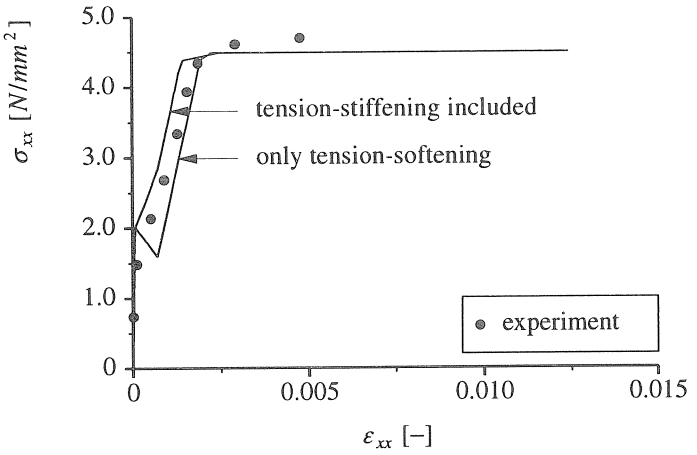

Figure 33 Influence of tension-stiffening on panel pb13 of Bhide and Collins.

The reinforcement in panel pb13 is applied in two grids with a reinforcement ratio given by $\rho_p = 0.01085$ and $\rho_q = 0.0$ and an angle $\psi = 0°$. The diameter of the deformed bars ϕ_p is equal to 6.55 [*mm*]. The material properties of panel pb13 are given in Table 7. The mean compressive strength of the concrete has been taken from the report of Bhide and Collins (1987) and the other material properties have been derived from this value with the formulas given in chapter 2. The effective tension area determined by the geometrical properties of the reinforcement is equal to 23.2 [*mm*] and the average crack spacing is equal to 100 [*mm*]. Compared with the experimental stabilized crack spacing of approximately 111 [*mm*], the calculated value of the average crack spacing is reasonably accurate. The nominal tensile stress-strain diagram of panel pb13 is shown in Figure 33. The influence of the tension-stiffening component in the constitutive model is obvious from this diagram. The calculated force at cracking of the panel is too high which indicates that the tensile strength of the concrete is overestimated. This also influences the tension-stiffening effect which has been chosen with a value equal to one.

Panel pb25 has been designed to study the effect of the amount of reinforcement and this panel is the companion specimen of panel pb13. The reinforcement ratio of panel pb25 is twice the reinforcement ratio of panel pb13, i.e. $\rho_p = 0.02170$ with the same angle $\psi = 0°$ and a diameter $\phi_p = 6.59$ [*mm*]. The reinforcement in the q-direction is again equal to zero. The material properties of panel pb25 are given in Table 8. The effective tension area determined by the geometrical properties of the reinforcement is equal to 23.2 [*mm*] and the average crack spacing equal to 66.5 [*mm*]. Compared with the experimental crack spacing of approximately 81 [*mm*], the calculated value of the average crack spacing is quite accurate. The nominal tensile stress-strain diagram of panel pb25 is shown in Figure 34. It is obvious from this diagram that the tension-softening component is more dominant for this panel than for panel pb13.

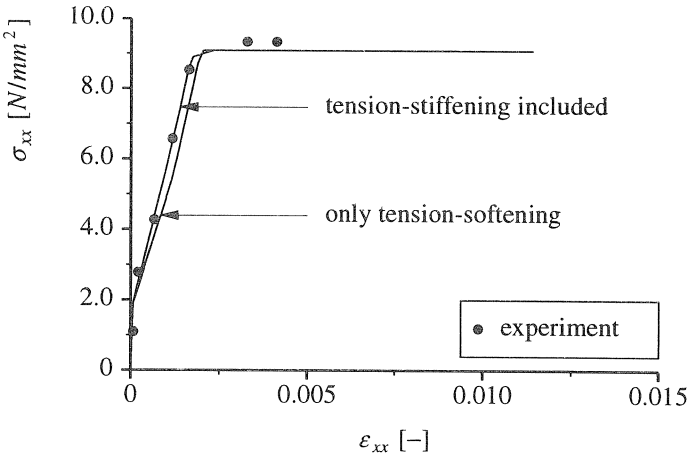

Figure 34 Influence of tension-stiffening on panel pb25 of Bhide and Collins.

Table 8 Material properties panel pb25.

concrete		
f_{cm}	20.0	[N/mm^2]
E_c	26000	[N/mm^2]
ν	0.15	[–]
$f_{ct,m}$	1.6	[N/mm^2]
G_f	0.06[1)]	[Nmm/mm^2]
reinforcement		
f_{sy}	414	[N/mm^2]
E_s	210000	[N/mm^2]

1) linear softening

The influence of the angle between a crack and the reinforcement has been studied with the analyses of two panels tested by Kollegger (1988). It concerns two panels with the same material properties and equal reinforcement, but with a different reinforcement angle ψ. Panel pk03 has an angle ψ equal to 0°, whereas panel pk04 has an angle 45°. The material properties are given in Table 9. The reinforcement ratio in p- and q-direction is equal to 0.0106 with a diameter of 6.5 [mm]. The effective tension area is equal to 23.1 [mm] and the average crack spacing equal to 100 [mm] for panel pk03 and an average crack spacing equal to 70 [mm] for panel pk04 which is in agreement with the experimental value of the stabilized crack spacing. The nominal stress-strain response in the x-direction of panel pk03 has been depicted in Figure 35 and that of panel pk04 is shown in Figure 36. The assumption that the tension-stiffening component acts in the direction of reinforcement is supported by the analyses of the panels

Table 9 Material properties panel pk03 and pk04.

concrete		
f_{cm}	20.0	$[N/mm^2]$
E_c	26000	$[N/mm^2]$
ν	0.15	[–]
$f_{ct,m}$	1.6	$[N/mm^2]$
G_f	0.06[1)]	$[Nmm/mm^2]$
reinforcement		
f_{sy}	700	$[N/mm^2]$
E_s	210000	$[N/mm^2]$

1) linear softening

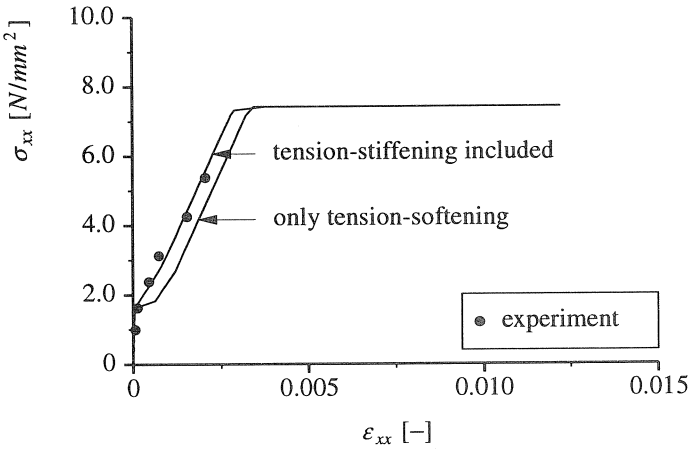

Figure 35 Influence of tension-stiffening on panel pk03 of Kollegger.

which show that the calculated behavior is close to the experimental behavior. The conclusion of Kollegger and Mehlhorn (1990b) that the influence of the angle between crack and reinforcement is negligible for the tension-stiffening model is confirmed by these analyses.

Finally, panel pv4 of Vecchio and Collins (1982) loaded in pure shear has been analyzed. Because of the isotropic reinforcement, the directions of the principal strain vector do not rotate and the behavior is completely determined by the tension-softening and tension-stiffening models. This panel is reinforced with two layers with a reinforcement ratio given by $\rho_p = \rho_q = 0.01056$ with a diameter $\phi_p = \phi_q = 3.45$ $[mm]$. The angle ψ between the reinforcement and the element axis is equal to 0°. The material properties

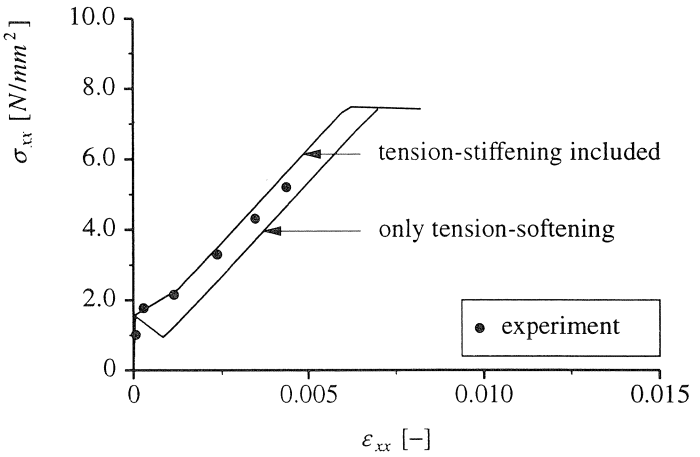

Figure 36 Influence of tension-stiffening on panel pk04 of Kollegger.

of panel pv4 are given in Table 10. The effective tension area is equal to 19.3 [*mm*] and the average crack spacing equal to 44.8 [*mm*]. The nominal shear stress-strain strain response of panel pv4 is shown in Figure 37. The behavior is in close agreement with the experimental behavior which shows yielding of the reinforcement.

Table 10 Material properties panel pv4.

concrete		
f_{cm}	26.0	[N/mm^2]
E_c	30000	[N/mm^2]
ν	0.15	[−]
$f_{ct,m}$	2.0	[N/mm^2]
G_f	0.06[1)]	[Nmm/mm^2]
reinforcement		
f_{sy}	242	[N/mm^2]
E_s	210000	[N/mm^2]

1) linear softening

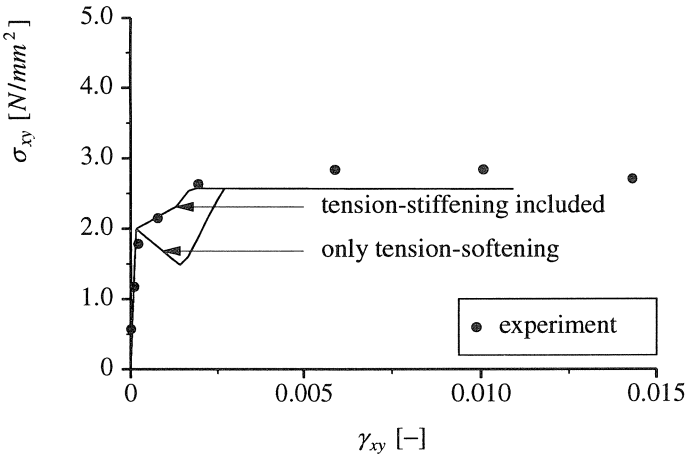

Figure 37 Influence of tension-stiffening on panel pv4 of Vecchio and Collins.

The next analyses will concern reinforced panels of Vecchio and Collins (1982) which are anisotropically reinforced. Due to this anisotropy, the direction of the principal strain will change after crack initiation. The degree of anisotropy is defined by the ratio of the potential yield loads of the reinforcement, Crisfield and Wills (1989), as

$$\omega_r = \frac{\rho_p \, f_{sy,p}}{\rho_q \, f_{sy,q}} \tag{47}$$

The analyses are performed with a single finite element configuration described previously and all panels are loaded in pure shear.

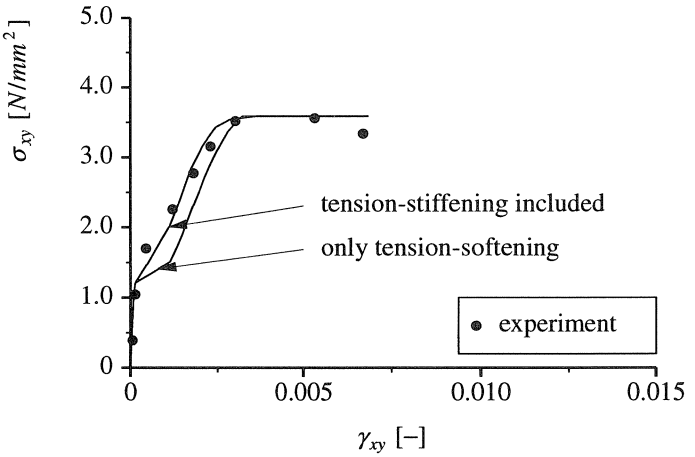

Figure 38 Influence of tension-stiffening on panel pv11 of Vecchio and Collins.

Table 11 Material properties panel pv11.

concrete		
f_{cm}	16.0	$[N/mm^2]$
E_c	25000	$[N/mm^2]$
ν	0.15	[–]
$f_{ct,m}$	1.2	$[N/mm^2]$
G_f	0.06[1)]	$[Nmm/mm^2]$
reinforcement		
f_{sy}	235	$[N/mm^2]$
E_s	210000	$[N/mm^2]$

1) linear softening

The first analysis concerns panel pv11 with a reinforcement ratio in the p-direction equal to 0.01785 with a diameter of 6.35 $[mm]$ and in the q-direction equal to 0.01306 with a diameter of 5.44 $[mm]$. This results in an anisotropy factor of the reinforcement $\omega_r = 1.37$. The reinforcement properties result in an effective tension area of 22.9 $[mm]$ in the p-direction and 21.8 $[mm]$ in the q-direction. The average crack spacing is equal to 51.5 $[mm]$ which is smaller than the experimentally observed crack spacing of 75 – 100 $[mm]$. The material properties are given in Table 11. The nominal shear stress-shear strain response is given in Figure 38. The agreement between analysis and experiment is reasonable if the tension-stiffening effect is taken into account. The tensile strength of 1.2 $[N/mm^2]$ which has been estimated by eq.(11) is lower than the experimentally observed tensile strength of approximately 1.6 $[N/mm^2]$. It is obvious in this case, with an anisotropy factor $\omega_r = 1.37$ that ignoring the shear resistance of the reinforced concrete is permitted.

The next panel concerns panel pv10 with an anisotropy factor $\omega_r = 1.79$. The reinforcement ratio in the p-direction is equal to 0.01785 with a diameter of 6.35 $[mm]$ and in the q-direction equal to 0.00999 with a diameter of 4.70 $[mm]$ which results in an effective tension area of 22.9 $[mm]$ in the p-direction and 20.8 $[mm]$ in the q-direction. The average crack spacing is equal to 51.4 $[mm]$ which is in agreement with the experimentally observed crack spacing of 50 – 75 $[mm]$. The material properties are given in Table 12. The nominal shear stress-shear strain response is given in Figure 39. The comparison of the analysis with the experiment shows that the tensile strength is again estimated too low, but that the resemblance is reasonable. The influence of the tension-stiffening component is small because the amount of ultimate crack strain is almost equal to the failure strain of the element.

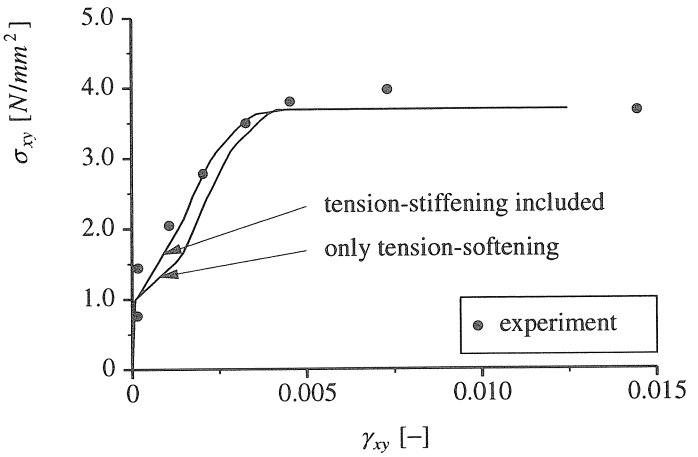

Figure 39 Influence of tension-stiffening on panel pv10 of Vecchio and Collins.

Table 12 Material properties panel pv10.

concrete		
f_{cm}	14.4	$[N/mm^2]$
E_c	24000	$[N/mm^2]$
ν	0.15	[–]
$f_{ct,m}$	1.0	$[N/mm^2]$
G_f	0.06[1)]	$[Nmm/mm^2]$
reinforcement		
f_{sy}	276	$[N/mm^2]$
E_s	210000	$[N/mm^2]$

1) linear softening

The next panel concerns panel pv19 where the anisotropy factor ω_r is equal to 3.83 which is large, considering the pure shear loading. The reinforcement is applied in two layers of reinforcing grids with a reinforcement ratio in the p-direction equal to 0.01785 with a diameter of 6.35 $[mm]$ and in the q-direction equal to 0.00713 with a diameter of 4.01 $[mm]$. These properties result in an effective tension area of 22.9 $[mm]$. The average crack spacing is equal to 51.4 $[mm]$ which is in agreement with the experimentally observed crack spacing of 50 – 75 $[mm]$. The yield stress of the reinforcing steel is different in the p- and q-directions, see Table 13. The nominal shear stress-shear strain response given in Figure 40 shows that the agreement with the experimental response is quite accurate, considering that the shear resistance is neglected.

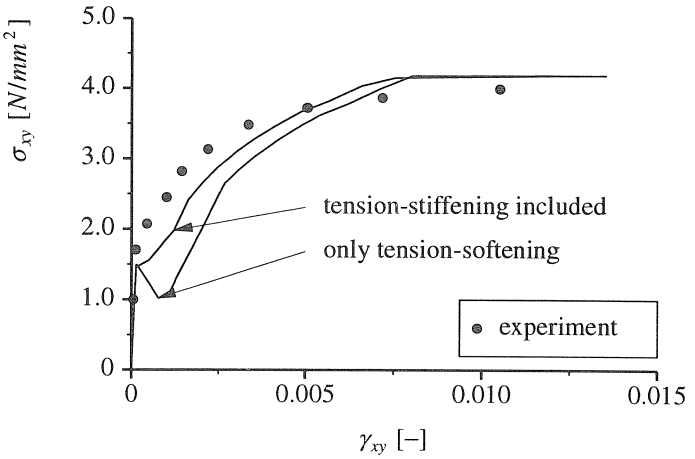

Figure 40 Influence of tension-stiffening on panel pv19 of Vecchio and Collins.

Table 13 Material properties panel pv19.

concrete		
f_{cm}	19.0	$[N/mm^2]$
E_c	26000	$[N/mm^2]$
ν	0.15	[–]
$f_{ct,m}$	1.5	$[N/mm^2]$
G_f	0.06[1)]	$[Nmm/mm^2]$
reinforcement		
$f_{sy,p}$	458	$[N/mm^2]$
$f_{sy,q}$	299	$[N/mm^2]$
E_s	210000	$[N/mm^2]$

1) linear softening

The final panel which will be analyzed is panel pv12 which has a large anisotropy factor $\omega_r = 6.98$. This large anisotropy factor produces a significant change in the principal strain directions. The reinforcement is applied in two layers of reinforcing grids with a reinforcement ratio in the p-direction equal to 0.01785 with a diameter of 6.35 $[mm]$ and in the q-direction equal to 0.00446 with a diameter of 3.18 $[mm]$. These properties result in an effective tension area of 22.4 $[mm]$. The average crack spacing is equal to 51.4 $[mm]$ which is in agreement with the experimentally observed crack spacing of $50 - 75$ $[mm]$. The yield stress of the reinforcing steel is different in the p- and q-direction, which are given in Table 14.

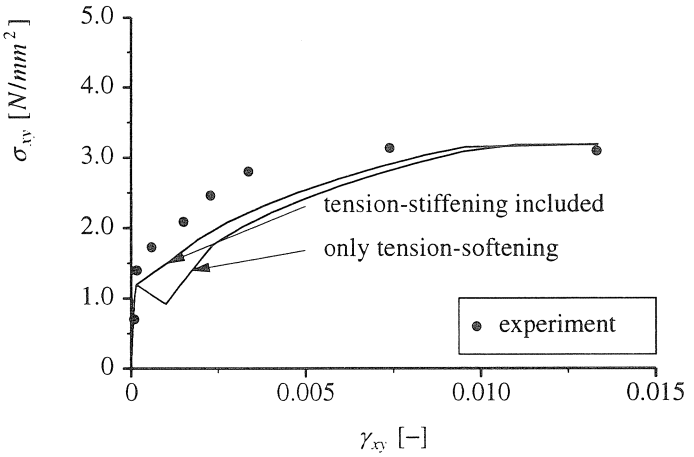

Figure 41 Influence of tension-stiffening on panel pv12 of Vecchio and Collins.

Table 14 Material properties panel pv12.

concrete		
f_{cm}	16.0	[N/mm^2]
E_c	25000	[N/mm^2]
ν	0.15	[−]
$f_{ct,m}$	1.2	[N/mm^2]
G_f	0.06[1)]	[Nmm/mm^2]
reinforcement		
$f_{sy,p}$	469	[N/mm^2]
$f_{sy,q}$	269	[N/mm^2]
E_s	210000	[N/mm^2]

1) linear softening

The nominal shear stress-shear strain response is given in Figure 41. It is clear from the analysis of panel pv12 that the shear resistance of the cracked reinforced concrete becomes more important if the directions of the principal strain vector change significantly. However the ultimate failure load is not affected if the failure mode is governed by yielding of the reinforcement.

It is concluded that neglecting the shear resistance of the cracked reinforced concrete is allowed as long as the anisotropy of the reinforcement is less than five and the loading is such that rotation of the principal directions can be expected. In cases where the structure is reinforced only in one direction, the Rankine plasticity model should be used with care, because the analysis might show a much too brittle response due to continuously rotation of the principal stress.

6. Application to reinforced concrete

The previous chapters have been addressed the two major problem areas in the modeling of reinforced structures, i.e. the development of a numerically stable model which deals with the biaxial stress states and the rational modeling of the tension-stiffening concept. In this chapter, two typical engineering problems will be presented which show the range of application of the developed models. The first example concerns the analyses of two deep beams without shear reinforcement which are designed to fail in compression. The proper modeling of the biaxial stress state is important for these type of structures. The second example concerns the analyses of shear wall panels in which both the biaxial stress state problems and the tension-stiffening problems will be encountered.

6.1 Analysis of deep beams

The analysis of deep beams is usually performed using an approach in which the structure is modeled using compressive struts and tensile ties. The experimental research program of Lehwalter (1988) was mainly concerned with the carrying-capacity of the compressive struts in this truss-model approach. The program consisted of two series of tests, the first series consisting of deep beams without shear reinforcement and the second series consisting of deep beam with shear reinforcement. The beams have a dense reinforced layer at the bottom of the beams which is designed such that the beams fail due to compressive failure without yielding of the reinforcement. Two beams of the first series have been selected, beam v023 with a depth over span ratio of 0.5, and beam v121 with a depth over span ratio of 1.0. Both beams have a thickness of 250 $[mm]$.

The first analysis concerns beam v023 with a depth of 360 $[mm]$ and a span of 720 $[mm]$. Only a half of the specimen has been modeled using 400 four-noded plane-stress elements with a four-point integration scheme. The reinforcement with a total area $A_s = 1020\ [mm^2]$ has been modeled using embedded bar elements. The developed model for the reinforced concrete has not been used in this analysis since it is believed that the concrete-reinforcement interaction does not have a large influence on the ultimate failure load of the structure. These examples have been selected to indicate the importance of the modeling of the biaxial stress state. The support platen has been modeled with eight four-noded plane-stress elements also with a four-point integration scheme. The finite element mesh is shown in Figure 42 and the material properties are given in Table 15.

The vertical displacement of the loading platen has been plotted against the load in Figure 43 in which the influence of compressive softening on the structural behavior is evident. If only cracking is taken into account, the analysis clearly shows first cracking and finally yielding of the reinforcement. The analysis with a composite yield surface shows that the nonlinear compressive behavior under the loading platen dominates the structural response.

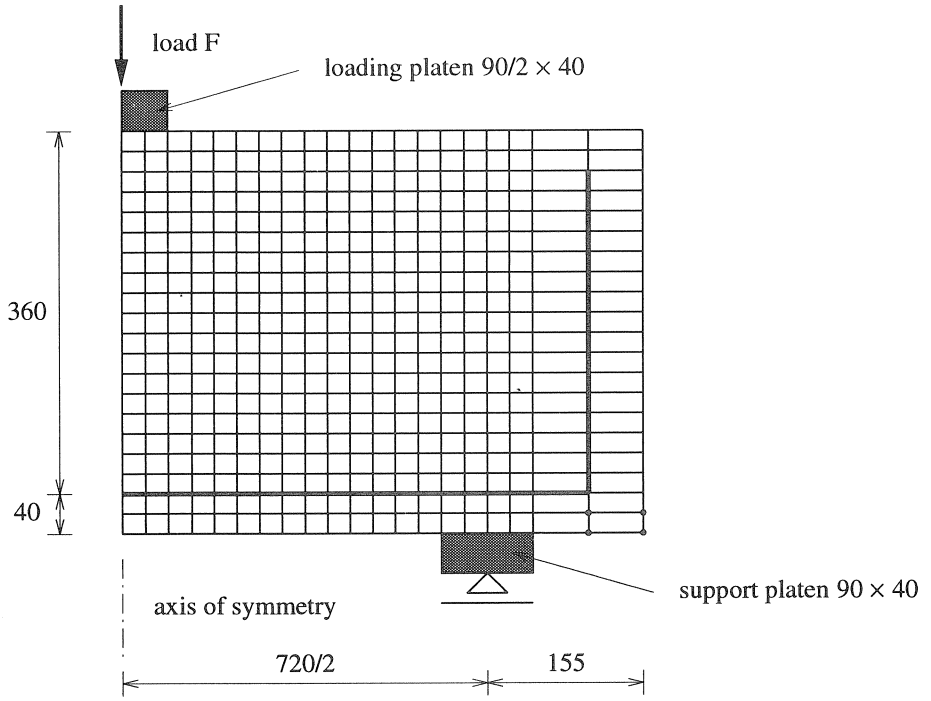

Figure 42 Deep beam v023 Lehwalter. Finite element mesh. Measures in [mm].

Table 15 Material properties deep beam v023.

	concrete	
f_{cm}	20.0	$[N/mm^2]$
E_c	30000	$[N/mm^2]$
ν	0.15	[–]
$f_{ct,m}$	2.0	$[N/mm^2]$
G_f	0.10[1)]	$[Nmm/mm^2]$
G_c	10.0[2)]	$[Nmm/mm^2]$
	reinforcement	
f_{sy}	420 – 500[3)]	$[N/mm^2]$
E_s	210000	$[N/mm^2]$

1) exponential softening
2) parabolic softening
3) hardening of steel with $\varepsilon_{sv} = 0.079$ [–]

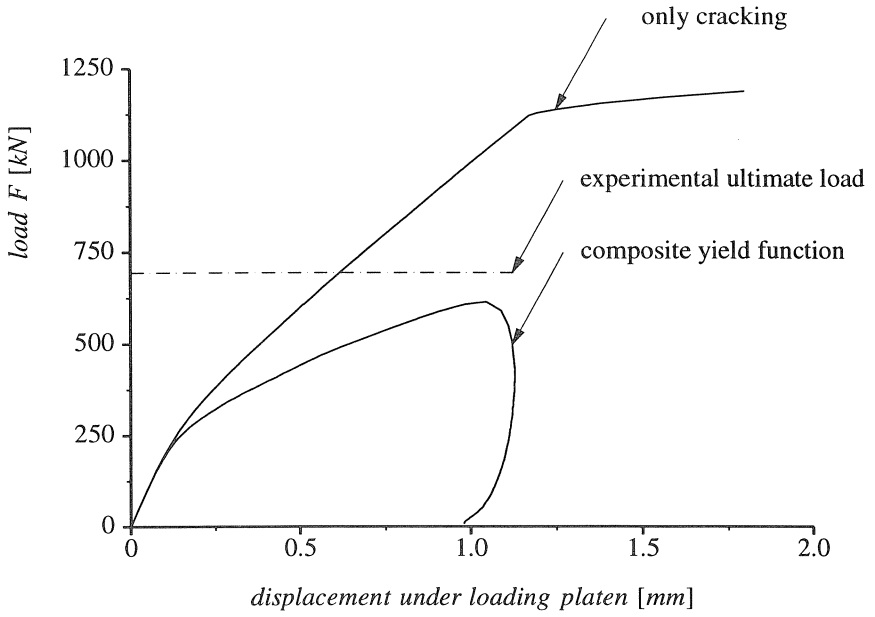

Figure 43 Deep beam v023 Lehwalter. Load - displacement diagram.

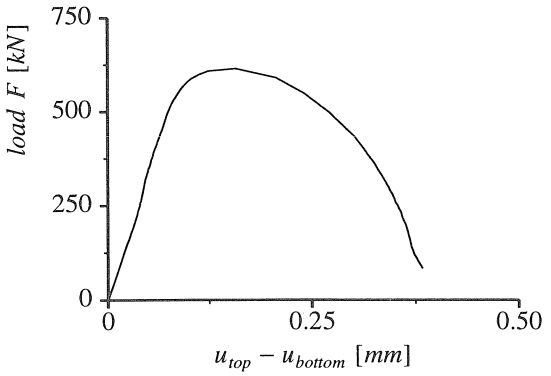

Figure 44 Deep beam v023 Lehwalter. Difference in the displacement of the midspan top and bottom of the beam.

The failure load which has been obtained in the analysis with a composite yield surface is in good agreement with the experimental failure load. The experimental load-deformation response has not been plotted because the measured response was inaccurate due to deformation of the supports, see Lehwalter (1988) and Walraven (1993). Only the experimental failure load has been indicated in Figure 43. The crack patterns

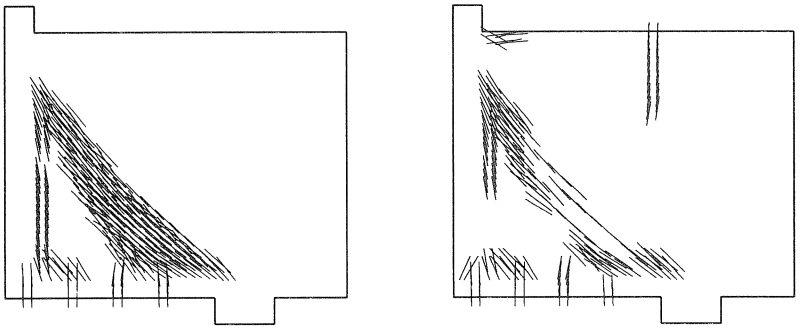

(a) (b)

Figure 45 Deep beam v023 Lehwalter. Crack pattern. (a) at maximum load ; (b) at final load

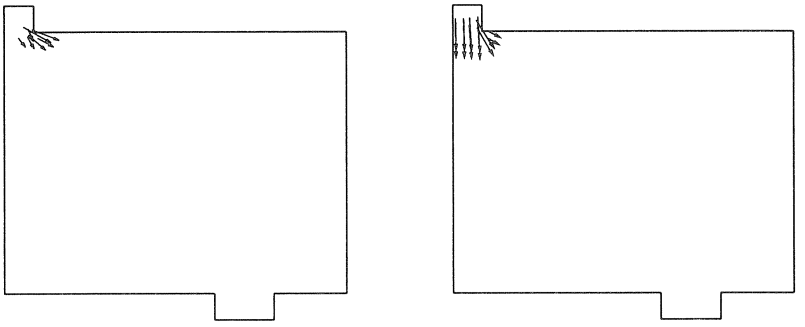

(a) (b)

Figure 46 Deep beam v023 Lehwalter. Compressive principal plastic strain. (a) at maximum load ; (b) at final load

which have been obtained with the composite yield surface are plotted in Figure 45. The distributed crack pattern around the reinforced area localizes in a dominant vertical crack. At a later stage the diagonal, densely cracked region develops. The crack pattern at the final stage shows that the diagonal cracks are closing while a vertical crack starts to develop above the support which has also been observed in the experiment. The compressive principal inelastic strain vectors depicted in Figure 46 shows that the failure mode is a local, compressive type of failure due to nonlinear compressive behavior. This is also clear from Figure 44 in which the difference between the displacement of the top and bottom at the midspan of the beam has been plotted. The load-displacement curve shows a monotonically increasing behavior, whereas the load-displacement curve

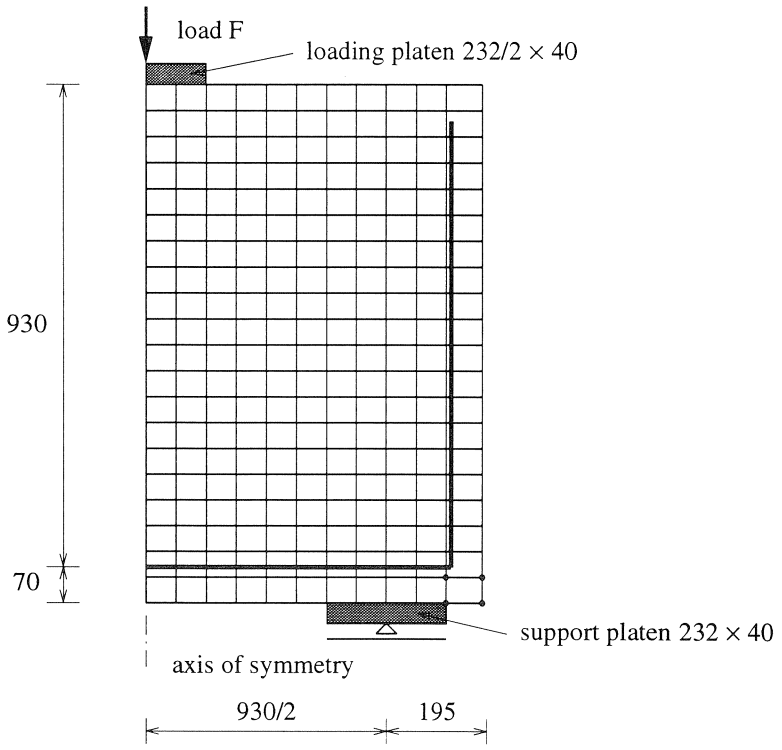

Figure 47 Deep beam v121 Lehwalter. Finite element mesh. Measures in [*mm*].

of the loading platen, depicted in Figure 43 shows a snap-back behavior. The structure unloads at the final stage, but the difference between the displacements under the loading platen and the bottom of the beam shows that we have an increasing deformation under the loading platen. The analysis of beam v023 shows that the behavior of the beam is governed by bending cracks and compression-shear cracks in the pre-peak regime. The ultimate failure mechanism is dominated by compressive softening under the loading platen, which results in a very brittle failure mechanism which is indicated by the snap-back in the load-displacement diagram. If only cracking is modeled, the ultimate failure mechanism is dominated by yielding of the reinforcement with an overestimation of the ultimate load with approximately a factor equal to 2, and results in a too ductile failure mechanism.

The second analysis concerns beam v121 with a depth of 930 [*mm*] and a span of 930 [*mm*]. Only half of the structure has been modeled using 220 four-noded plane-stress elements with a four-point integration scheme. The reinforcement has been modeled using embedded bar elements. The support platens have been modeled with four four-noded plane-stress elements also with a four-point integration scheme. The finite

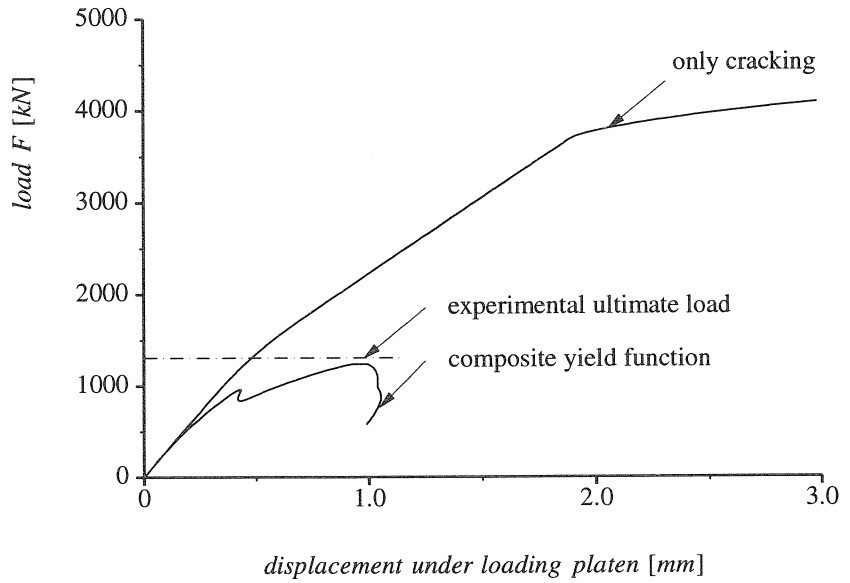

Figure 48 Deep beam v121 Lehwalter. Load - displacement diagram.

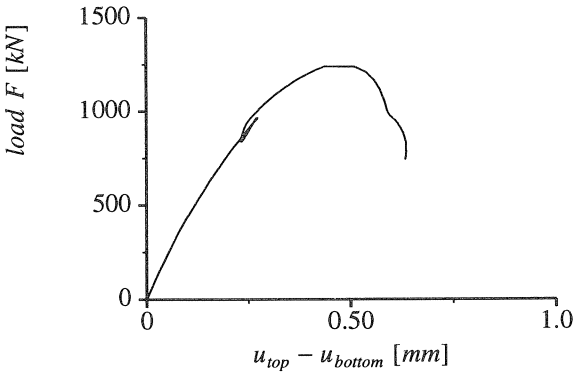

Figure 49 Deep beam v121 Lehwalter. Difference in the displacement of the midspan top and bottom of the beam.

element mesh is depicted in Figure 47, and the material properties are equal to the material properties of beam v023 which have been given in Table 15. Again, the vertical displacement of the loading platen has been plotted against the applied load in Figure 48 in which the influence of compressive softening on the structural behavior is even more evident than for the previous structure. If only cracking is taken into account, the analysis shows a decrease in the stiffness due to cracking and finally yielding of the

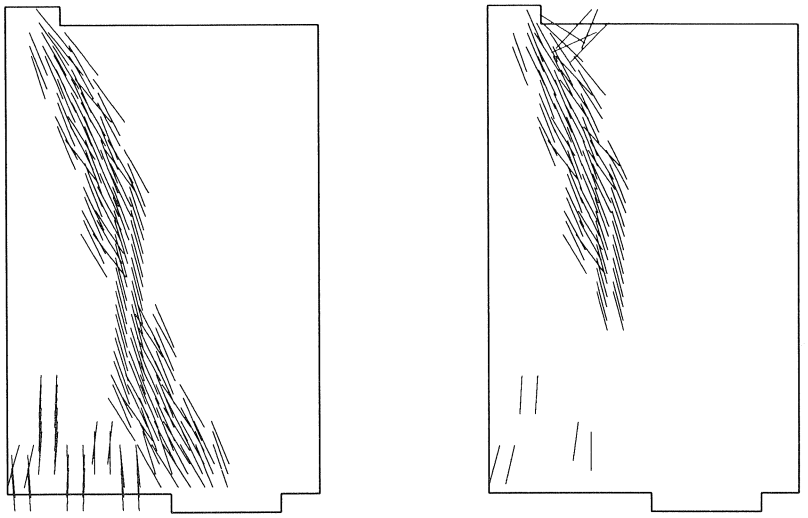

Figure 50 Deep beam v121 Lehwalter. Crack pattern (a) at maximum load ; (b) at final load

reinforcement. The analysis with a composite yield surface shows that the nonlinear compressive behavior under the loading platen results in a large decrease of the maximum load and that it is important to incorporate compressive softening in order to accurately predict the failure load of these types of deep beams. The calculated failure load is in good agreement with the experimental failure load which have been plotted in Figure 48. Again, only the maximum experimental failure load has been plotted, since the load-deflection curve which has been measured is inaccurate because of displacements of the supports. The difference between the displacement of the loading platen and the deflection of the midspan of the beam is shown in Figure 49. The calculated crack pattern which is shown in Figure 50, indicates that the structure is mainly subjected to a compression-shear loading, because the bending cracks are less dominant than in the previous structure. At the maximum load we observe some small bending cracks in the middle of the structure with a dominant shear-type crack pattern in the compressive strut. The failure mode is governed by the compressive softening under the loading platen which is shown in Figure 51. This local failure mechanism causes an unloading of the structure which has also been observed in the previous example.

The two analyses of the deep beams show the major influence of compressive softening on the structural failure mechanism.

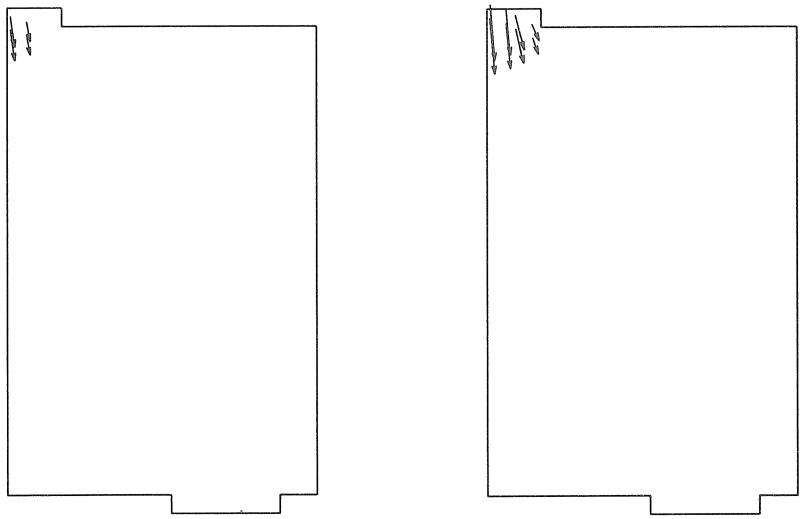

Figure 51 Deep beam v121 Lehwalter. Compressive principal plastic strain. (a) at maximum load ; (b) at final load

6.2 Analysis of shear wall panels

The analysis of shear wall panels is a good example of the possible application of the developed models. The stress state in the panels can be considered to be in tension-compression. The panels are usually reinforced by a reinforcing grid which makes the examples also a good indicator for the influence of the tension-stiffening on the behavior of the panels. The panels which will be presented in this study have been tested at the E.T.H. Zürich by Maier and Thürlimann (1985) and have been analyzed before with the finite element package DIANA by Wang, Van der Vorm and Blaauwendraad (1990). The constitutive model which has been used in that study is a combination of a fixed crack model to describe the tensile stress state and a Mohr-Coulomb plasticity model to describe the compressive stress states, see for details about this constitutive model Van der Vorm (1988). However, the combination of cracking and plasticity resulted in convergence problems if a large region existed in which both the cracking and the plasticity model became active. These numerical problems were solved by defining two areas in which either only the cracking model or only the plasticity model could become active. The solutions which were obtained with this approach are in good agreement with the experimental results which indicates that the method is rather effective. The arbitrariness of defining the regions a-priori is a major draw-back of this method and the analyses with the combined yield surface presented here will show that the convergence problems are avoided if a stable algorithm is used to describe the constitutive behavior. The experimental program of Maier and Thürlimann (1986), concerned a series of 10 shear

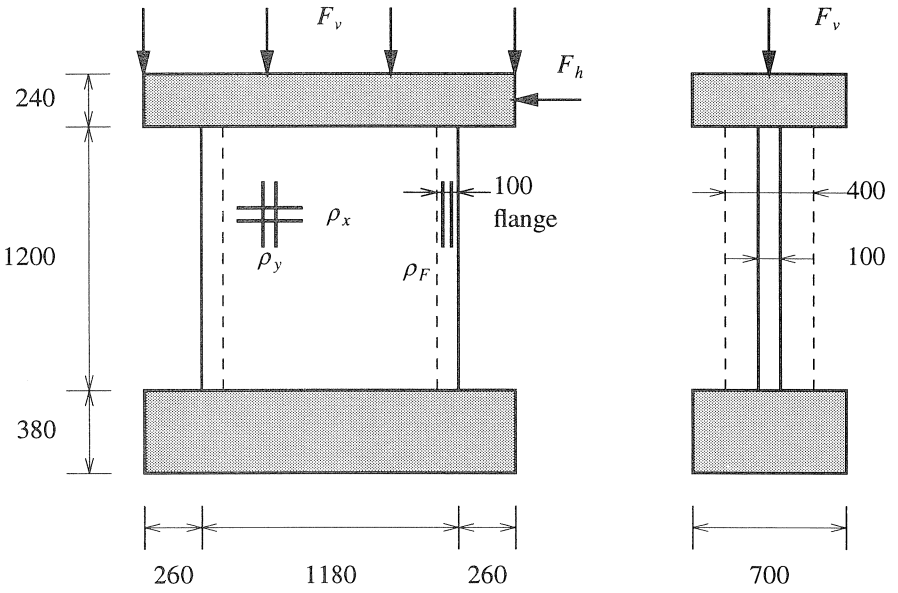

Figure 52 Experimental set-up. Measures in [*mm*].

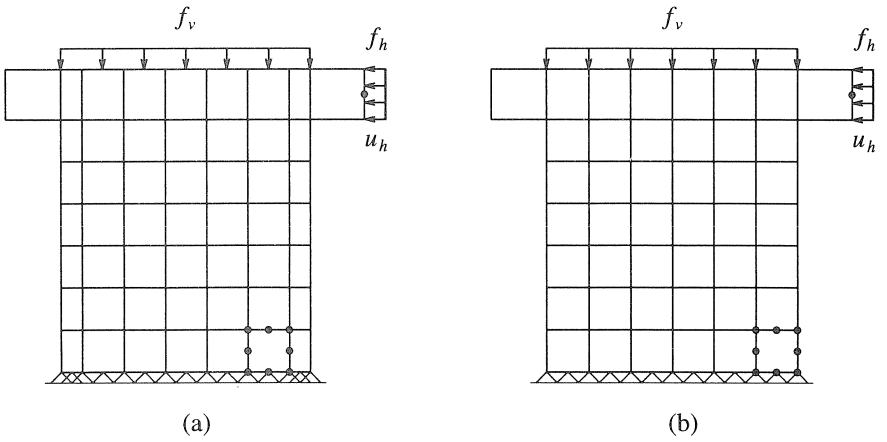

Figure 53 Finite element discretization panels Maier and Thürlimann (1985). a) panels S1 and S2 ; b) panels S4 and S10

wall panels with flanges and panels without flanges. The panels are all loaded initially by a vertical compressive force, and then loaded by a horizontal force until the experiment became unstable and the failure load had been reached. The experimental set-up is shown in Figure 52, with the panels supported on a base block and loaded through a thick top slab.

Table 16 Material properties panels Maier and Thürlimann (1985).

concrete		
f_{cm}	27.5	$[N/mm^2]$
E_c	30000	$[N/mm^2]$
ν	0.15	[–]
$f_{ct,m}$	2.2	$[N/mm^2]$
G_f	0.07[1)]	$[Nmm/mm^2]$
G_c	50.0[2)]	$[Nmm/mm^2]$
reinforcement		
f_{sy}	574 – 764[3)]	$[N/mm^2]$
E_s	200000	$[N/mm^2]$

1) linear softening
2) parabolic softening
3) hardening of steel with $\varepsilon_{sy} = 24.6\ 10^{-3}$ [–]

Four panels from the series, S1, S2, S4 and S10, have been analyzed with the composite plasticity model and the influence of the tension-stiffening component on the behavior has been examined. The material properties have been averaged from the experimental data of the four panels provided by Thürlimann and Maier (1986) with a reduction of the compressive strength of 20 %. The material properties which have been used in the analyses are given in Table 16. The material properties have been averaged in order to simulate the behavior of the panels in a qualitative manner. In this way, it is better possible to study the influence of the different reinforcement ratio, initial vertical stress and geometry. The reinforcement is applied by reinforcing grids in two directions with a diameter of 8 $[mm]$ and a clear cover of 10 $[mm]$. The reinforcement ratios and the initial vertical force are given in Table 17.

Table 17 Reinforcement and vertical load of panels Maier and Thürlimann (1985).

Panel	ρ_x $[10^{-3}]$	ρ_y $[10^{-3}]$	ρ_F $[10^{-3}]$	F_v $[kN]$
S1	10.3	11.6	11.6	–433
S2	10.3	11.6	11.6	–1653
S4	10.3	10.5	10.5	–262
S10	9.8	10.0	57.1[1)]	–262

1) additional reinforcement in tension area over 197 $[mm]$

The finite element discretizations of the panels are depicted in Figure 53 with quadratic plane-stress elements with a nine-point Gaussian integration for both the reinforcement and the element. The reinforcement has been applied in two layers of a reinforcing grid. The top slab has been modeled with linear-elastic elements without reinforcement, whereas the supporting block has been replaced by fixed supports in the x- and y-

direction. The additional reinforcement in panel S10 has not been applied in an area of 240 [*mm*] as in the experiments, but has been applied in the first element at the tension side, i.e. over a length of 197 [*mm*].

The horizontal and vertical load have been applied as a uniformly distributed element load as indicated in Figure 53. The horizontal displacement u_h of the top slab has been monitored and compared with the experimental load-displacement curves. Initially, the solution technique with the constrained Newton-Raphson iteration with line searches has been applied to analyze the panels. It happened that it was not possible to achieve converged solutions after the maximum load and therefore the indirect displacement control method without line searches has been used to analyze these panels, see Feenstra (1993). The displacement in the horizontal direction u_h has been chosen as the active degree-of-freedom with load steps of approximately 0.2 [*mm*]. With this solution technique, converged solutions could be obtained in the complete loading regime.

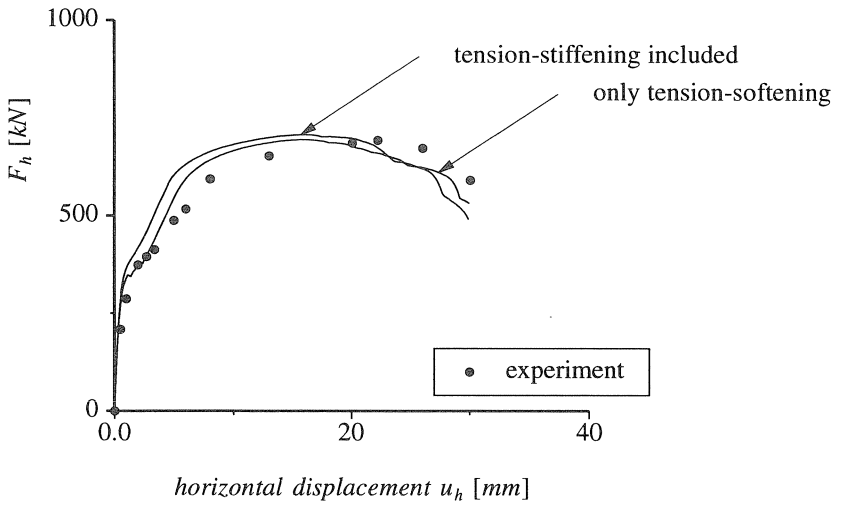

Figure 54 Panel S1. Load - displacement diagram.

The first panel which will be presented is a panel with flanges which will be denoted as panel S1. This panel is subjected to an initial vertical load of 433 $[kN] \equiv 2.5\ [N/mm^2]$ which results in an initial horizontal displacement of 0.06 [*mm*] in the experiment. The calculated initial displacement is equal to $-80 \cdot 10^{-6}$ [*mm*] which indicates a possible eccentricity in the experimental set-up. After the initial vertical load, the horizontal load is applied with indirect displacement control. The load-displacement diagram of panel S1 is shown in Figure 54, which shows a reasonable agreement between experimental and calculated response. The influence of the tension-stiffening component on the load-displacement diagram is small, but inclusion of the tension-stiffening avoids some numerical difficulties which are related to local

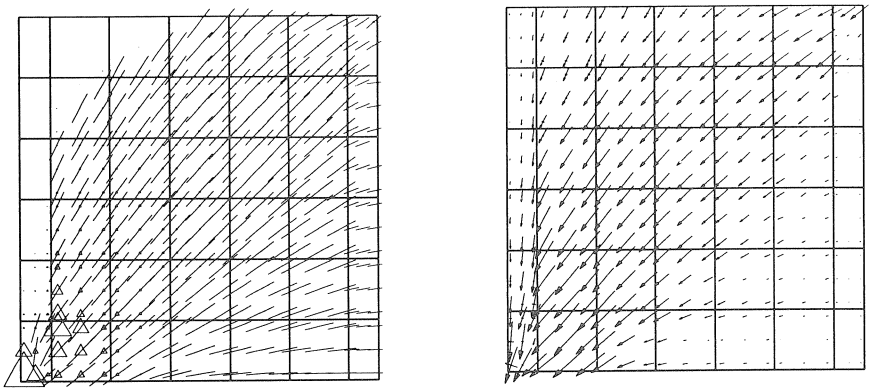

(a) (b)

Figure 55 Panel S1. Results of the analysis at a displacement of 10 [*mm*]. (a) active cracks and plastic points ; (b) principal stresses.

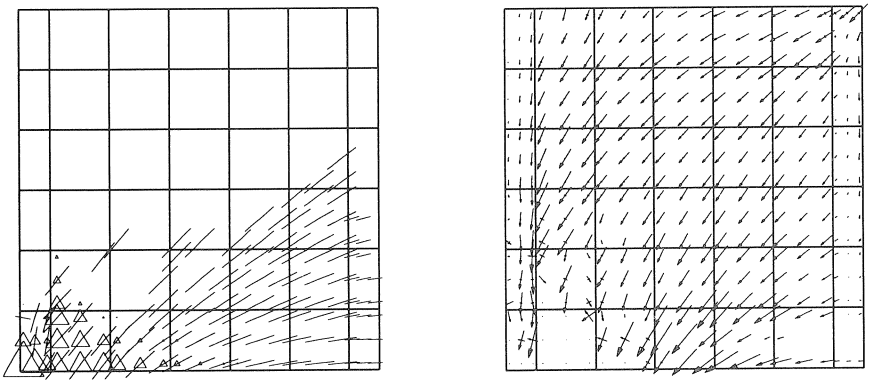

(a) (b)

Figure 56 Panel S1. Results of the analysis at a displacement of 30 [*mm*]. (a) active cracks and plastic points ; (b) principal stresses.

maxima due to crack localization in the pre-peak regime. The results of the analysis will be presented by plotting the active cracks with a line and the integration points which are in a compressive plastic state are depicted with a triangle. The size of the triangle is proportional with the magnitude of the internal parameter. Furthermore, the principal stresses are depicted which are in general compressive. The active cracks are defined as those cracks for which the internal parameter κ is equal or greater than $0.5\,\kappa_u$. The

results for panel S1 at a displacement of the top slab of 10 [*mm*] are shown in Figure 55. The panel is densely cracked with plastic points in the bottom-left corner of the panel. The concrete in the bottom-right corner does not transfer any stress anymore as can be seen from Figure 55(b). The load carrying mechanism through a compressive strut can clearly be observed from the principal stresses. The results of panel S1 at the final displacement of 30 [*mm*] show the failure mechanism which is governed by compressive softening of the concrete and yielding of the reinforcing steel both in tension and compression, see Figure 56. In the ultimate state, the concrete in the bottom-left corner transfers no stress anymore, which is in agreement with the experimentally observed failure mechanism where the concrete was crushed in the bottom-left corner of the panel and in the flange at the compression side.

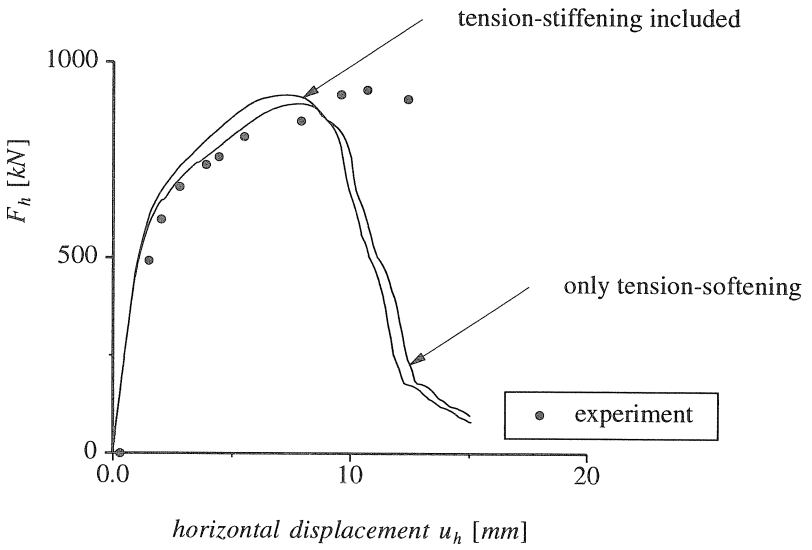

Figure 57 Panel S2. Load - displacement diagram.

Panel S2 is identical with the previous panel, but the initial vertical load is approximately four times the initial stress in panel S1, which increases the ultimate load of the structure but decreases the ductility of the panel dramatically, see Figure 57. The agreement between the ultimate load of the experiment and the calculated maximum load is good. The influence of the additional stiffness caused by the inclusion of the tension-stiffening component is small. The experimental initial displacement of the experiment is quite large, which could not be simulated. The experimental failure mechanism was rather explosive and caused a complete loss of load-carrying capacity which can be explained by the brittle behavior of the panel after maximum load, see Figure 57. The results of the analysis at a displacement u_h equal to 5 [*mm*], see Figure 58, show that the panel is heavily cracked with plastic points in the bottom-left corner of the panel and in

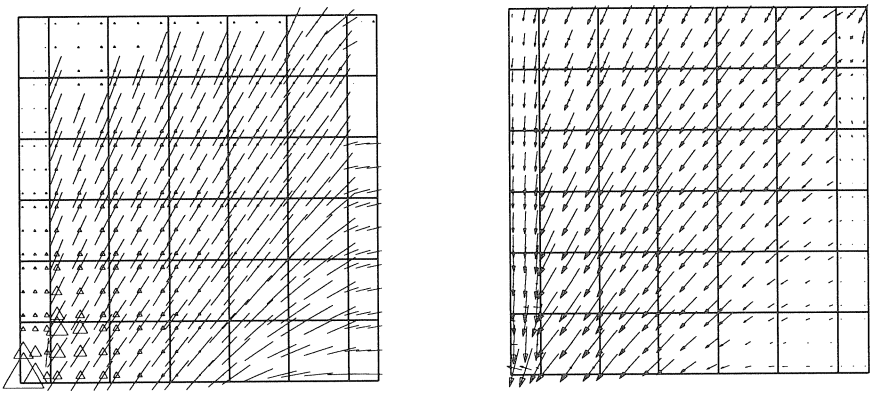

(a) (b)

Figure 58 Panel S2. Results of the analysis at a displacement of 5 [*mm*]. (a) active cracks and plastic points ; (b) principal stresses.

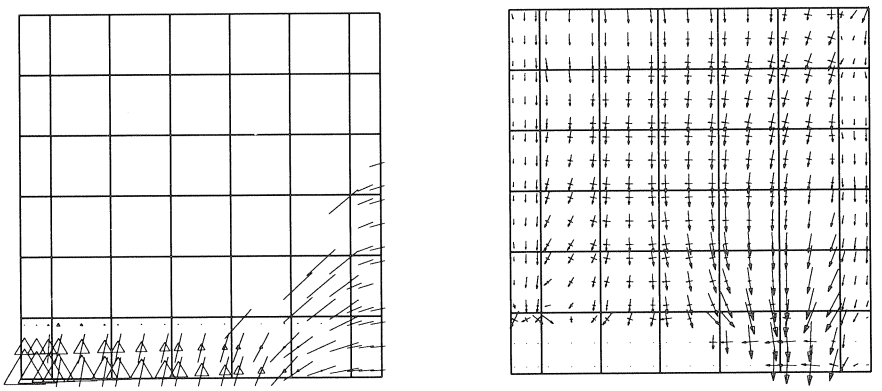

(a) (b)

Figure 59 Panel S2. Results of the analysis at a displacement of 15 [*mm*]. (a) active cracks and plastic points ; (b) principal stresses.

the compressive flange. The results of panel S2 at the ultimate displacement u_h of 15 [*mm*] are shown in Figure 59 in which the redistribution of internal forces in the panel can clearly be observed. The complete loss of stiffness in the bottom of the panel can be seen from Figure 59 which is combined with yielding of the reinforcement in compression. The reinforcement in the tension flange also yields, but this is less dominant.

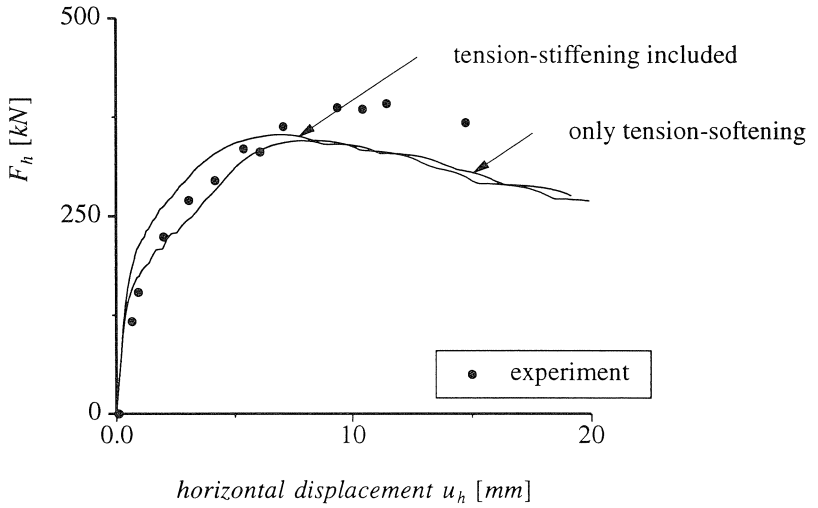

Figure 60 Panel S4. Load - displacement diagram.

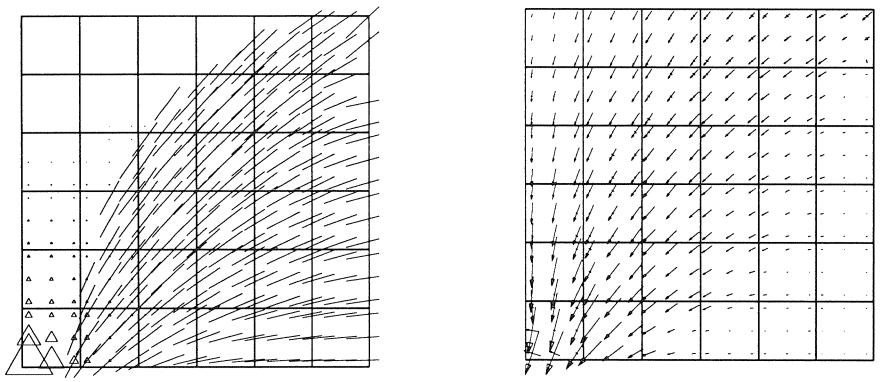

Figure 61 Panel S4. Results of the analysis at a displacement of 5 [*mm*]. (a) active cracks and plastic points ; (b) principal stresses.

Panel S4, which will be analyzed next, is the equivalent of panel S1 without flanges. The initial vertical force of 262 [*kN*] results in approximately the same vertical stresses as in panel S1. The load-displacement diagram is given in Figure 59 which again shows a reasonable agreement between the ultimate loads of the experiment and of the analysis. The influence of the tension-stiffening component is more dominant and results in a

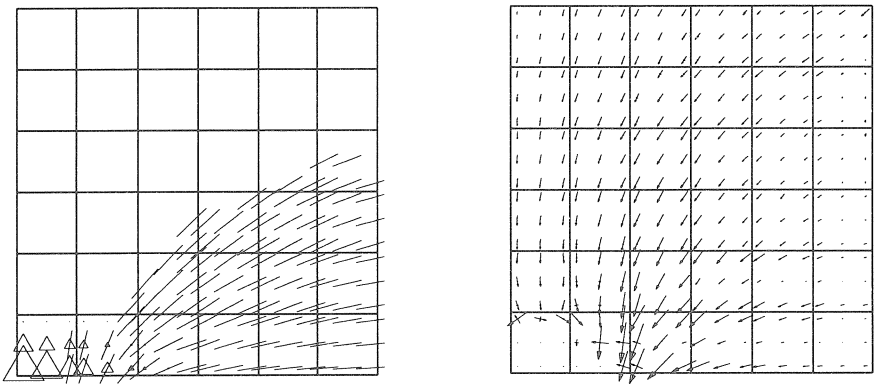

(a) (b)

Figure 62 Panel S4. Results of the analysis at a displacement of 20 [*mm*]. (a) active cracks and plastic points ; (b) principal stresses.

more stable numerical solution than if the tension-stiffening component is neglected. In this case convergence could only be achieved with small steps in the ascending branch until a stabilized crack pattern has been achieved. The panel behaves in a rather ductile manner after peak load which has also been observed in the experiment where the horizontal displacement could be increased approximately 30 % after the ultimate load had been reached. The results of the analysis are shown in Figures 61 and 62 at a horizontal displacement u_h of 5 [*mm*] and 20 [*mm*] respectively. The experimentally observed failure mode is related to crushing of the concrete in a region in the bottom-left part of the panel. This failure mechanism can also be observed from Figure 62(a) and (b), because the principal stresses at the bottom-left corner of the panel are almost reduced to zero.

The final panel which will be analyzed, is a panel with a "hidden tensile flange". In the tension side of the panel, additional reinforcement has been applied which increases the ultimate load, compared with panel S4, but results in a less ductile behavior, see Figure 63. The agreement between the experimental and calculated ultimate load is quite reasonable, but the calculated initial stiffness exceeds the experimental initial stiffness with approximately a factor equal to two. Also the displacement at the failure load is too small compared with the experimental displacement. The results of the analysis of panel S10, given in Figures 64 and 65, show the differences with the results of panel S4, mainly in the post-peak regime. The active cracks and plastic points as well as the direction of the principal compressive strut are almost equal for both panel S4 and S10, compare Figure 61 and Figure 64. The results at a displacement of 20 [*mm*] show a considerable different behavior between panel S4 and panel S10. The part of panel S10 in which the stresses are reduced to zero is much larger than the region in panel S4 which

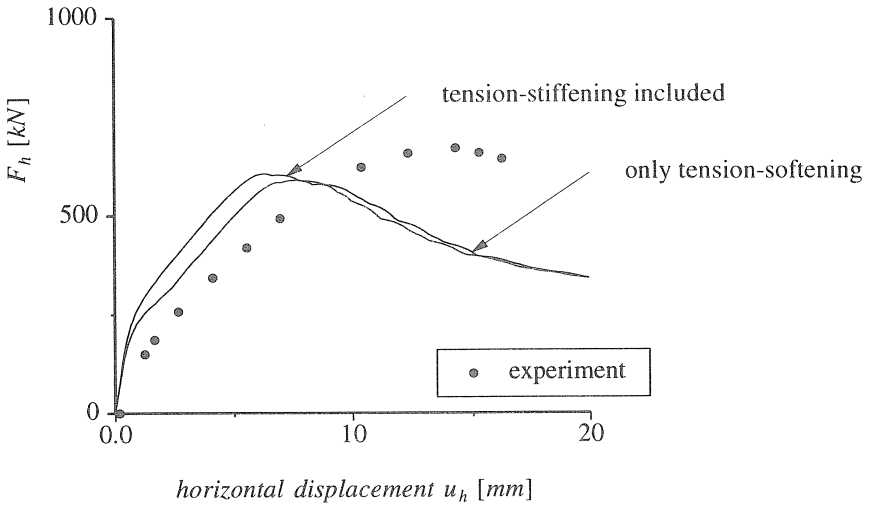

Figure 63 Panel S10. Load - displacement diagram.

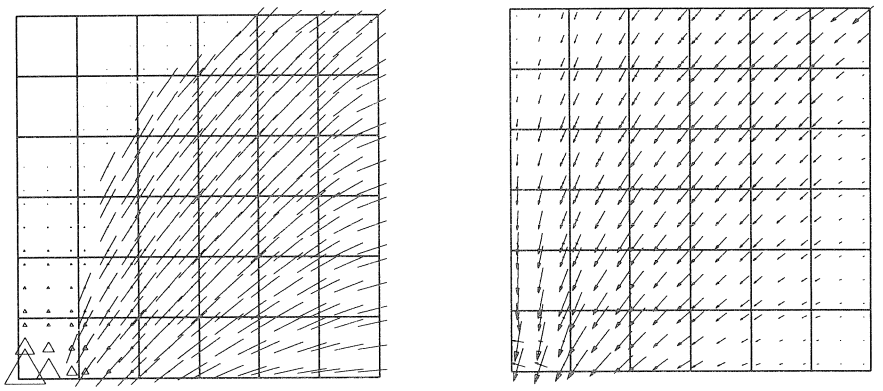

(a) (b)

Figure 64 Panel S10. Results of the analysis at a displacement of 5 [*mm*]. (a) active cracks and plastic points ; (b) principal stresses.

has also been observed in the experiments, see Figure 62 and 65.

In conclusion, it has been shown that the agreement between the experimental and numerical results is good, and that the experimental failure mechanism can be simulated with the composite plasticity model. The influence of the modeling of the tension-stiffening component on the load-displacement curve is in general small, but inclusion of it can result in a more stable iterative procedure in the pre-peak regime.

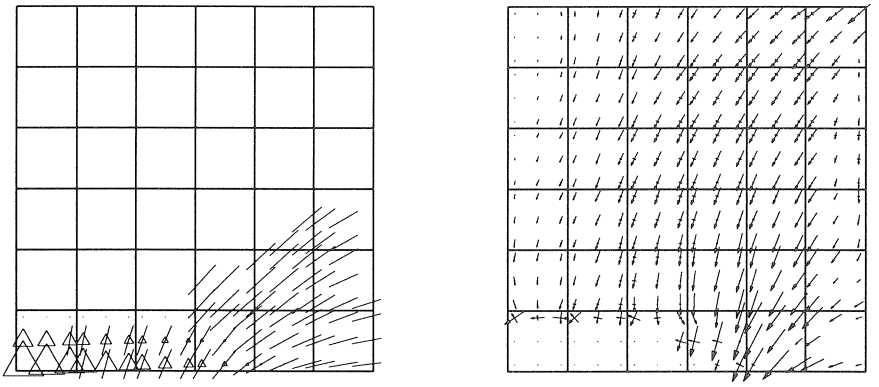

(a) (b)

Figure 65 Panel S10. Results of the analysis at a displacement of 20 [*mm*]. (a) active cracks and plastic points ; (b) principal stresses.

7. Summary and concluding remarks

The structural engineer more and more needs reliable numerical tools to analyze the post-failure behavior of structures in order to assess the structural safety. In general, a reliable numerical tool consists of an accurate material description in combination with a robust solution strategy. In this study an attempt has been made to provide such a tool for the analyses of reinforced concrete structures.

A material model for plain and reinforced concrete in a plane-stress situation has been discussed. It is assumed that the failure mechanism of concrete loaded in tension and compression is governed by crack growth at the micro-level. Furthermore it is assumed that the internal damage caused by these micro-cracks can be modeled using internal parameters which are related to a fracture energy in tension and to a fracture energy in compression. The material properties have been estimated using CEB-FIP recommendations which are based on the compressive strength of the concrete. The comparisons between numerical analyses with material properties based on these recommendations and experiments show that estimated material properties are adequate. The biaxial behavior of concrete is assumed to be governed by the failure surface of Kupfer and Gerstle with a tension-softening and a compression-softening constitutive behavior.

The mechanical response of reinforced concrete is assumed to be given by a superposition of the elasto-plastic behavior of the reinforcement, the tension-softening behavior of the plain concrete and an additional stiffness due the interaction between concrete and reinforcement. The total amount of fracture energy due to distributed cracking is assessed using the average crack spacing based on CEB-FIP recommendations. For the biaxial behavior of reinforced concrete the biaxial loaded reinforced panels of Kollegger

and Mehlhorn have been used. It is not obvious from these experiments that the compressive strength should be reduced as a function of lateral cracking, since a constant reduction can be observed. This phenomenon is possibly a result of the size effect and the influence of different boundary conditions in the standard compression test and the actual experiment.

The constitutive model of plain concrete can be formulated in an incremental fashion or within a total strain concept. The rotating crack model falls within the latter category. In the former group of models, two fracture energy-based plasticity models have been presented, the Rankine plasticity model and a composite yield function which governs the entire range of biaxial stress states. The models have been compared with a fundamental tension-shear model problem which indicates that the constitutive behavior of the Rankine plasticity model and the rotating crack model shows much resemblance. The models have been applied to different structures and a comparison between the numerical and experimental results indicates that the most promising material model for concrete is the Rankine plasticity model. Application of the composite plasticity model to reinforced concrete structures in which biaxial stress states are prominent, shows that the composite plasticity model results in a stable and accurate procedure. The entire pre- and post-failure regime can be traced in a stable manner, which gives a good impression of the failure characteristics of these type of structures.

Ackowledgements

The calculations have been carried out with the DIANA finite element code of TNO Building and Construction Research. The financial support by the Netherlands Technology Foundation (STW) under grant DCT-72.1405 and by the Commission of the European Communities through the Brite-Euram program (project BE-3275) is gratefully acknowledged.

References

ARREA, M. and INGRAFFEA, A.R. (1982) - Mixed-mode crack propagation in mortar and concrete. Report 81-13, Cornell University, New York, USA.

BAŽANT, Z.P. and OH, B.H. (1983) - Crack band theory for fracture of concrete. *Materials and Structures,* RILEM, **93(16)** , p. 155-177.

BHIDE, S.B. and COLLINS, M.P. (1987) - Reinforced concrete elements in shear and

tension. Publication 87-02, University of Toronto, Canada.

BRAAM, C.R. (1990) - Control of crack width in deep reinforced concrete beams. Dissertation, Delft University of Technology, The Netherlands.

CEB-FIP (1990) - Model code 1990. Bulletin d'information, CEB.

CERVENKA, V., PUKL, R. and ELIGEHAUSEN, R. (1990) Computer simulation of anchoring technique in reinforced concrete beams, in: *Computer Aided Analysis and Design of Concrete Structures,* eds. N. Bićanić et al., Pineridge Press, p. 1-21.

CHEN, W.F. (1982) - *Plasticity in reinforced concrete.* McGraw-Hill.

CRISFIELD, M.A. (1984) - Difficulties with current numerical models for reinforced concrete and some tentative solutions, in: *Computer Aided Analysis and Design of Concrete Structures,* , eds. F. Damjanić et al., Pineridge Press, p. 331-358.

CRISFIELD, M.A. and WILLS, J. (1989) - Analysis of R/C panels using different concrete models. *J. Engrg. Mech.,* ASCE, **115(3)** , p. 578-597.

DE BORST, R. (1986) - Non-linear analysis of frictional materials. Dissertation, Delft University of Technology, The Netherlands.

DE BORST, R. and NAUTA, P. (1985) - Non-orthogonal cracks in a smeared finite element model. *Engrg. Comput.,* **2** , p. 35-46.

ELFGREN, L. (1990) - Round-robin analysis of anchor bolts. Invitation. *Materials and Structures,* RILEM, **23(133)** , p. 78.

FEENSTRA, P.H., ROTS, J.G. and DE BORST, R. (1990) - Round robin analysis of anchor bolts. Report 25.2-90-5-07, Delft University of Technology, The Netherlands.

FEENSTRA, P.H., DE BORST and R. ROTS, J.G. (1991a) - Numerical study on crack dilatancy. I: Models and stability analysis. *J. Engrg. Mech.,* ASCE, **117(4)** , p. 733-753.

FEENSTRA, P.H., DE BORST and R. ROTS, J.G. (1991b) - Numerical study on crack dilatancy. II: Applications. *J. Engrg. Mech.,* ASCE, **117(4)** , p. 754-769.

GAMBAROVA, P.G. (1987) - Modelling of interface problems in reinforced concrete, in: *IABSE Report, vol. 54,* Delft University Press, p. 1-16.

HANNANT, D.J., BUCKLEY, K.J. and CROFT, J. (1973) - The effect of aggregate size on the use of the cylinder splitting test as a measure of tensile strength. *Materials and Structures,* RILEM, **6(31)** , p. 15-21.

HORDIJK, D.A. (1991) - Local approach to fatigue of concrete. Dissertation, Delft University of Technology, The Netherlands.

KOLLEGGER, J. (1988) - Ein Materialmodell für die Berechnung von Stahlbetonflächentragwerken. Dissertation, Gesamthochschule Kassel, Germany.

KOLLEGGER, J. and MEHLHORN, G. (1990a) - Experimentelle Untersuchungen zur Bestimmung der Druckfestigkeit des gerissenen Stahlbetons bei einer Querzugbeanspruchung. Heft 413, Deutscher Ausschuß für Stahlbeton, Germany.

KOLLEGGER, J. and MEHLHORN, G. (1990b) - Material model for the analysis of reinforced concrete surface structures. *Comp. Mech.,* **6** , p. 341-357.

KUPFER, H.B. and GERSTLE, K.H. (1973) - Behavior of concrete under biaxial stresses. *J. Engrg. Mech.,* ASCE, **99(4)** , p. 853-866.

LABBANE, M., SAHA, N.S. and TING, E.C. (1993) - Yield criterion and loading function for concrete plasticity. *Int.J.Solids Structures,* **30(9)** , p. 1269-1288.

LEHWALTER, N. (1988) - Die Tragfähigkeit von Betondruckstreben in Fachwerkmodellen am Beispiel von Gedrungenen Balken. Dissertation, Technischen Hochschule Darmstadt, Germany.

MAIER, J. and THÜRLIMANN, B. (1985) - Bruchversuche an Stahlbetonscheiben. Report 8003-1, Eidgenössische Technische Hochschule Zürich, Switzerland.

NELISSEN, L.J.M. (1972) - Biaxial testing of normal concrete. *Heron* **18** , p. 3-90.

OLIVER, J. (1989) - A consistent characteristic length for smeared crack models. *Int. J. Numer. Methods Engrg.,* **28** , p. 461-474.

PRAMONO, E. and WILLAM, K.J. (1989) - Implicit integration of composite yield surfaces with corners. *Engrg. Comput.,* **7** , p. 186-197.

ROTS, J.G. (1988) - Computational modeling of concrete fracture. Dissertation, Delft University of Technology, The Netherlands.

ROTS, J.G. (1992) - Removal of finite elements in strain-softening analysis of tensile fracture, in *Fracture mechanics of concrete structures,* ed. Z.P. Bažant, Elsevier Applied Science, p. 330-338.

SAOURIDES. C. and MAZARS, J. (1989) - A multiscale approach to distributed damage and its usefulness for capturing structural size effect, in *Cracking and damage. Strain localization and size effect,* eds. J. Mazars and Z.P. Bažant, Elsevier Applied Science, p. 391-403.

SCHLANGEN, E. (1993) - Experimental and numerical analysis of fracture processes in concrete. Dissertation, Delft University of Technology, The Netherlands.

SIMO, J.C., KENNEDY, J.G. and GOVINDJEE, S. (1988) - Non-smooth multisurface plasticity and viscoplasticity. Loading/unloading conditions and numerical algorithms. *Int. J. Numer. Methods Engrg.,* **26** , p. 2161-2185.

VAN DER VORM, P.L.J. (1988) - A numerical study on reinforced concrete panels. Report and appendices, Delft University of Technology, The Netherlands.

VAN MIER, J.G.M. (1984) - Strain-softening of concrete under multiaxial loading conditions. Dissertation, Eindhoven University of Technology, The Netherlands.

VECCHIO, F.J. and COLLINS, M.P. (1982) - The response of reinforced concrete to in-plane shear and normal stresses. Publication 82-03, University of Toronto, Canada.

VECCHIO, F.J. and NIETO, M. (1991) - Shear-friction tests on reinforced concrete panels. *J. ACI,* ACI, **88(3)** , p.371-379.

VERVUURT, A., SCHLANGEN, E. and VAN MIER, J. (1993) - A numerical and experimental analysis of the pull-out behavior of steel anchors embedded in concrete. Report 25.5-93-1, Delft University of Technology, The Netherlands.

VONK, R.A. (1992) - Softening of concrete loaded in compression. Dissertation, Eindhoven University of Technology, The Netherlands.

WALRAVEN, J.C. and REINHARDT (1981) - Theory and experiments on the mechanical behaviour of cracks in plain and reinforced concrete subjected to shear loading. *Heron,* **26(1a)** , p. 3-68.

WALRAVEN, J.C. (1993) - Private communications.

WANG, Q.B., VAN DER VORM, P.L.J. and BLAAUWENDRAAD, J. (1990) - Failure of reinforced concrete panels - How accurate the models must be ?, in: *Computer Aided Analysis and Design of Concrete Structures,* eds. N. Bićanić et al., Pineridge Press, p. 153-163.

WILLAM, K.J., PRAMONO, E. and STURE, S. (1986) - Fundamental issues of smeared crack models, in *Proc. SEM/RILEM Int. Conf. Fracture of Concrete and Rock,* eds. S.P. Shah and S.E. Swartz, Springer-Verlag, p. 142-157.

WITTMAN, F.H. (1983) - Structure of concrete with respect to crack formation, in *Fracture mechanics of concrete,* ed. F.H. Wittman, Elsevier, p. 43-74.